# Edinger-Westphal peptidergic neurons enable maternal preparatory nesting

Thomas Topilko, Silvina L Diaz, Catarina M Pacheco, Florine Verny, Charly V Rousseau, Christoph Kirst, Charlotte Deleuze, Patricia Gaspar, Nicolas M Renier

HAL Id: hal-03561422

https://hal.sorbonne-universite.fr/hal-03561422v1

Submitted on 8 Feb 2022

# Edinger-Westphal peptidergic neurons enable maternal preparatory nesting

## Graphical abstract
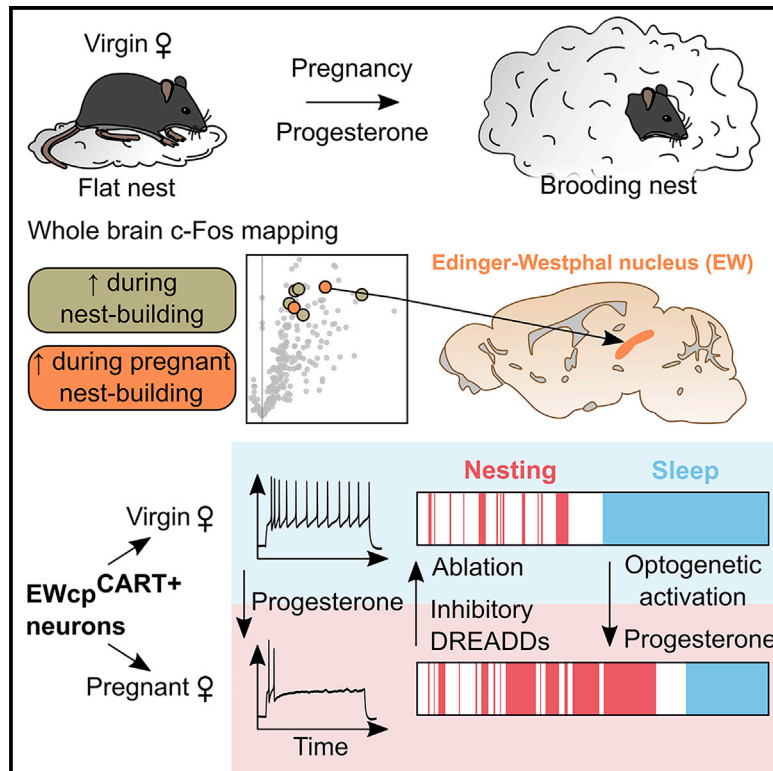


## Authors

Thomas Topilko, Silvina L. Diaz, Catarina M. Pacheco, ..., Charlotte Deleuze, Patricia Gaspar, Nicolas Renier

## Correspondence

nicolas.renier@icm-institute.org

## In brief

Pregnancy hormones modulate many behaviors ensuring the survival of the upcoming litter. Topilko et al. describe a poorly studied population of midbrain peptidergic neurons that is sensitive to progesterone and is necessary for the onset of maternal preparatory nest building during pregnancy, before the pups are born.

## Highlights

- Maternal preparatory nesting elicits activity in the EW nucleus

- Peptidergic EW neurons are necessary for maternal preparatory nesting

- Progesterone alters peptidergic EW neuron firing and triggers preparatory nesting

- Peptidergic EW neurons project to and modulate many regions controlling nesting

CellPress

# Neuron

CellPress
OPEN ACCESS

## Article

# Edinger-Westphal peptidergic neurons enable maternal preparatory nesting

Thomas Topilko,[1] Silvina L. Diaz,[1,2] Catarina M. Pacheco,[1] Florine Verny,[1] Charly V. Rousseau,[1] Christoph Kirst,[1,3] Charlotte Deleuze,[1] Patricia Gaspar,[1] and Nicolas Renier[1,4,*]

[1]Sorbonne Université, Paris Brain Institute - ICM, INSERM, CNRS, AP-HP, Hôpital de la Pitié Salpêtrière, Paris, France
[2]Consejo Nacional de Investigaciones Científicas y Técnicas (CONICET) Instituto de Biología Celular y Neurociencia Prof. E de Robertis (IBCN), Facultad de Medicina, Universidad de Buenos Aires (UBA), Ciudad Autónoma de Buenos Aires, Argentina
[3]Present address: Kavli Institute for Fundamental Neuroscience, Department of Anatomy, UCSF, San Francisco, and Lawrence Berkeley National Laboratory, Berkeley, CA, USA
[4]Lead contact
*Correspondence: nicolas.renier@icm-institute.org
https://doi.org/10.1016/j.neuron.2022.01.012

## SUMMARY

Optimizing reproductive fitness in mammalians requires behavioral adaptations during pregnancy. Maternal preparatory nesting is an essential behavior for the survival of the upcoming litter. Brain-wide immediate early gene mapping in mice evoked by nesting sequences revealed that phases of nest construction strongly activate peptidergic neurons of the Edinger-Westphal nucleus in pregnant mice. Genetic ablation, bidirectional neuromodulation, and *in vitro* and *in vivo* activity recordings demonstrated that these neurons are essential to modulate arousal before sleep to promote nesting specifically. We show that these neurons enable the behavioral effects of progesterone on preparatory nesting by modulating a broad network of downstream targets. Our study deciphers the role of midbrain CART+ neurons in behavioral adaptations during pregnancy vital for reproductive fitness.

## INTRODUCTION

Reproduction is essential for the continuation of species. As for many processes crucial for survival, the brain plays a central role in optimizing reproductive fitness. Therefore, the reproductive state profoundly impacts animal behaviors through the hormonal modulation of neuronal circuits (Bridges, 2016; Brunton and Russell, 2008; Kohl et al., 2017). For instance, hormones such as progesterone, estrogens, and prolactin modulate the properties of several classes of neurons in the hypothalamic preoptic area during late pregnancy and delivery to prime the brain for maternal behaviors (Keller et al., 2019; Kohl, 2020; Kohl and Dulac, 2018).

A wide range of behavioral adaptations during pregnancy are present in all mammalian females (Bridges, 2016; Brunton and Russell, 2008). In rodents, these adaptations include lowered anxiety (Neumann et al., 1998), increased feeding (Johnstone and Higuchi, 2001), modified thermoregulation (Smarr et al., 2016), increased nest building (Lisk et al., 1969), and sleep (Komiya et al., 2018). These behavioral changes affect the animal's daily routine during pregnancy, as well as its social interactions. Pregnancy strongly enhances nesting activity in mice, in a phenomenon known as "preparatory nesting" that anticipates providing a thermal and physical shelter for the upcoming litter before the pups are born (Lisk et al., 1969). The neural mecha-

nisms regulating this survival trait and how it is modulated by hormones are unknown.

In laboratory settings, mice reorganize their nest daily: in the dark phase, the nest is disorganized by the normal activities of mice but is rebuilt in the same location at the beginning of the light phase before rest (Jirkof, 2014; Jirkof et al., 2013). As a result, nest building happens at the start of a behavioral sequence, which consists of nesting, grooming, and then sleep (Eban-Rothschild et al., 2016, 2017; Sotelo, 2022). We reasoned that preparatory nesting could modify profoundly some of the essential behaviors in the daily routine of pregnant females. We thus aimed to describe how maternal preparatory nesting emerges during pregnancy in the mouse.

In this study, we identified the Edinger-Westphal (EW) nucleus as a region involved in the control of nesting, with a specific importance for preparatory nesting during pregnancy. The EW nucleus is mainly known for its control of the ciliary reflex (Ranson and Magoun, 1933). However, the region also contains a diverse set of midline neurons expressing a wide array of neuropeptides including urocortin 1 (UCN1), cholecystochinine (CCK), and cocaine- and amphetamine-regulated transcript (CART) (Giardino et al., 2012; Pomrenze et al., 2021; Zuniga and Ryabinin, 2020). Injection of tracers showed that these midline neurons project to many different brain regions, both rostrally and caudally, and constitute what is known as the "centrally
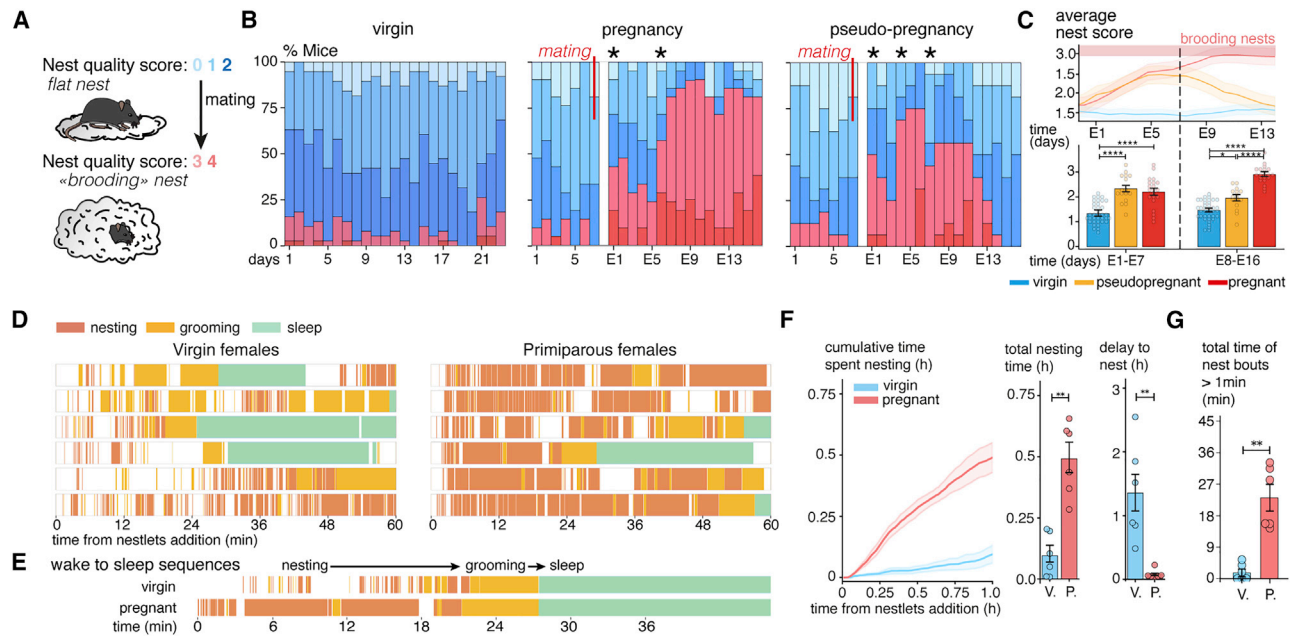
**Neuron**
Article



**Figure 1. Preparatory nesting is a plastic behavior enabled by the elongation of nesting bouts in wake-to-sleep sequences**

(A) Nests are scored from 0 to 4 based on their height: 0 to 2 for open nests and 3 and 4 for closed "brooding" nests. Then, 95% of mid-gestational females build brooding nests over 2/3$^{rd}$ of days.

(B) Daily proportions of nest scores in a cohort of C57BL/6NRj mice. After mating, the proportion of preparatory nests increases in both pregnant and pseudopregnant mice. Nest quality returns to baseline in pseudopregnant mice 13 days after mating. *Indicates days for which the mean nest scores are significantly different from those in the previous day (p < 0.05, Wilcoxon signed rank test).

(C) Rolling average curve of the mean daily nest score of virgin, pseudopregnant, and pregnant mice, and the mean score calculated for each mice in the first and second weeks of pregnancy is shown.

(D) Event plots of nesting, grooming, and sleep behaviors recorded after the addition of nestlets in virgin and pregnant mice at E15 (each row is a mouse, the first hour after the initiation of nesting is shown). Nesting bouts are longer and occupy most of the active time in pregnant females.

(E) Detail of a wake-to-sleep behavioral sequence in a virgin and an E15 pregnant mice. While the grooming bouts are comparable in both mice, nesting bouts are extended in pregnant females.

(F) Cumulative curve of nest time based on (D). E15 pregnant females initiate nesting sooner and spend more time nesting than virgin females.

(G) Comparisons of the overall uninterrupted nesting time (bouts of 1 min or more) of virgin and pregnant females. E15 pregnant females maintain long uninterrupted nesting bouts. ** P < 0.01 and **** P < 0.0001. Unpaired Mann-Whitney ranked U test (A, F, and G) and one-way ANOVA Kruskal-Wallis test (C). All data are presented as mean ± SEM. See also Figure S1 and Video S1.

projecting EW" (EWcp), distinct from the cholinergic peripherally projecting neurons (Dos Santos Júnior et al., 2015; Kozicz et al., 2011). Recently, behavioral studies have shown that the activity of murine EWcp neurons increases arousal during tasks involving conditioning (Lovett-Barron et al., 2017), memorization (Li et al., 2018), or fear modulation (Priest et al., 2021). Moreover, neurons of this region control the transitions between sleep phases (Zhang et al., 2019). Here, we show that the peptidergic neurons of the EWcp nucleus are also essential for the hormonal control of preparatory nesting during pregnancy.

## RESULTS

### Preparatory nesting is a plastic behavior enabled by the elongation of nesting bouts in wake-to-sleep sequences

We scored nest quality daily in C57BL/6NRj inbred mice based on height (Deacon, 2006) (Figures 1A and S1A). In virgin mice, the average nest quality was low (cohort score: 1.5 ± 0.04, n = 38 mice) but increased strongly the day following mating with another significant increase 5 to 7 days after (Figure 1B). From

the second gestational week onward, 95% of the pregnant mice had transitioned to consistently building preparatory nests (over at least 4 days in this week, cohort score: 2.9 ± 0.1, n = 21 mice) (Figures 1A and 1B). In females mated with vasectomized males, an increase in the frequency of high nesting scores was seen between embryonic day 1 (E1) and E11, which subsequently receded to baseline (Figures 1B and S1C). In complete pregnancies, high nesting scores eventually also receded to baseline after the weaning of the litter (Figure S1D). These results show that the capacity to build preparatory nests in female mice is a plastic behavioral adaptation primarily under the control of the animal's reproductive status. Conversely, while the nesting baseline in sexually naive animals was higher in males than in females (2.3 ± 0.1 versus 1.5 ± 0.04, p < 0.0001, Figure S1G), mating in males did not affect their nesting scores (2.3 ± 0.1 versus 2.2 ± 0.1 after mating, p = 0.62, n = 5 mice/group) (Figures S1E and S1F), showing that preparatory nesting after mating is a female-specific behavior.

To quantify nesting adaptations during pregnancy, we recorded the behavior after adding fresh nesting material until
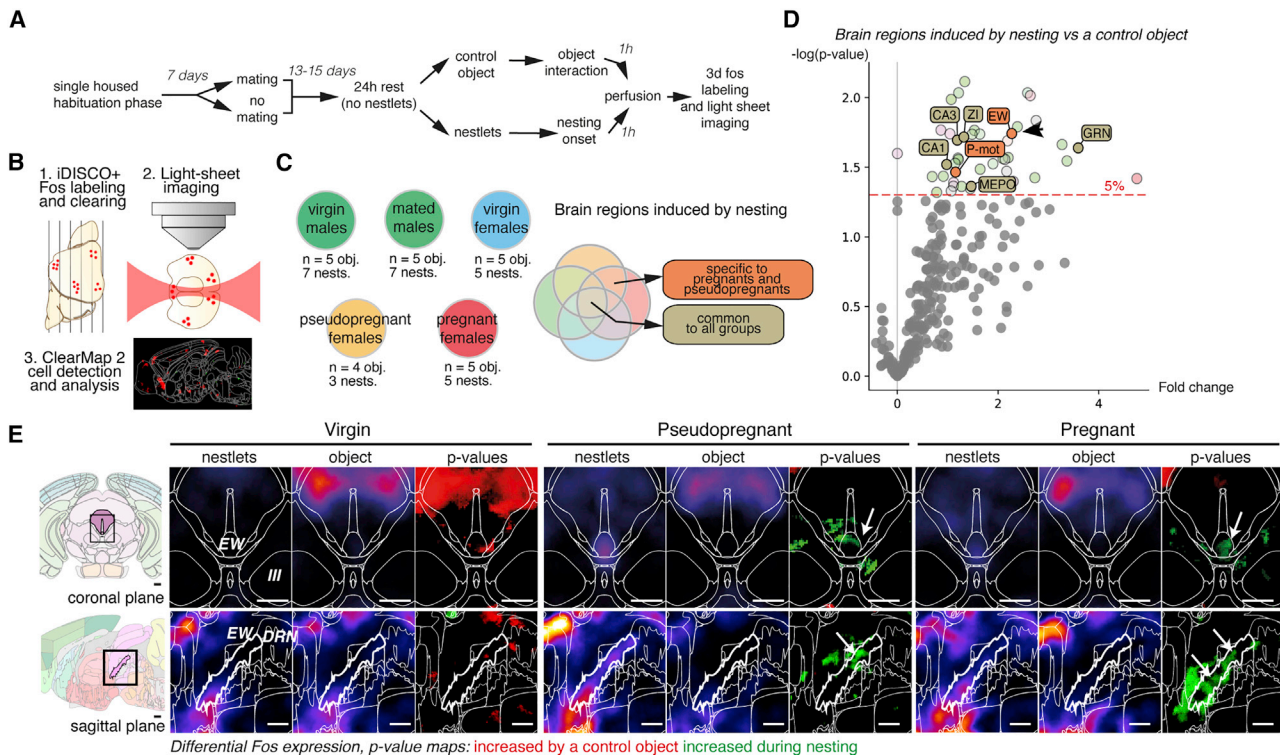
**CellPress**
OPEN ACCESS



Figure 2. Brain-wide search identifies the peptidergic neurons of the EW nucleus as selectively more active in pregnant female nest builders

(A) Strategy to map activity-dependent Fos expression in nest builders.

(B) Generation of statistical maps of Fos+ cell distribution using iDISCO+ clearing and light sheet microscopy.

(C) Design of the different experimental groups: five groups of two conditions were considered for the comparative study of nesting-induced regions. Two types of induced regions are further considered: nesting-induced regions found in all groups (greige) and regions specific to both pregnant and pseudopregnant mice (orange).

(D) Volcano plot of nesting-induced regions in pregnant females as fold change in Fos+ cells (nest builders over controls). Significant regions appearing in all nest builder groups are the MEPO, GRN, ZI, and CA1, and CA3 (tancolored). Significant regions present only in pregnant and pseudopregnant animals are the motor pontine formation and the EW nucleus.

(E) Coronal and sagittal views of the p value of the voxel maps of Fos+ cell densities at the level of the EW nucleus in virgin, pseudopregnant, and pregnant female mice, showing the presence of significant voxels of induced cells (green, arrows) in the EW nucleus only in pregnant and pseudopregnant animals. Student's t test (C and D). Scale bars are 500 μm. See also Figure S2.

1 h after nesting onset (Figures 1D, 1E, and S1B). Pregnant females at E14–E15 exhibited more prolonged bouts of nest building than virgins (Figures 1F and 1G: 61 ± 12 s versus 18 ± 3 s, n = 6 mice/group, p = 0.0022), with shorter latencies to initiate nesting (4.7 ± 1.8 min versus 81.3 ± 18.8 min, p = 0.0022) (Figure 1F; Video S1) and longer overall time (29.5 ± 3.7 min versus 5.4 ± 2.2 min over 1 h, n = 6 mice/group, p = 0.0022). The duration of grooming episodes was unchanged in pregnant females (57 ± 13 s versus 37 ± 13 s, p = 0.31) (Figure 1D). These observations show that pregnancy strongly increases the time allotted to nest building in the wake-to-sleep sequence (Figure 1E).

## Brain-wide Fos maps identify the peptidergic neurons of the EW nucleus as selectively more active in pregnant female nest builders

We searched for the brain activity signature of nesting specific to pregnant females. For this, we performed a screen based on the whole-brain expression of the immediate early gene Fos, using iDISCO+ and ClearMap (Renier et al., 2016) (Figure 2A). After

habituation to handling, half of a cohort of male and female mice was mated. At 14 to 15 days after mating, we further split the groups into two test conditions, in which the mice received either only the control object or fresh nesting material. Mice were perfused 1 h after the onset of nesting and processed for 3D Fos immunolabeling and light sheet imaging (Figure 2B). This experiment generated 5 groups (females: virgin, pseudopregnant, and pregnant; males: virgin and mated) with two test conditions each (nestlets or objects) (Figure 2C). We generated a list of brain regions that were significantly more active in nesting mice over the control condition for each group. Two sets of regions retained our interest: (1) regions active during nesting across all groups and (2) regions more active during nesting in pseudopregnant and pregnant groups (Figure 2C). Among the regions induced across all nest builders were the zona incerta, the median preoptic areas, the brainstem reticular formation, and the CA fields of the hippocampus (Figures 2D and S2A). Only two regions were exclusively significantly more active in pregnant and pseudopregnant groups during nest building: the
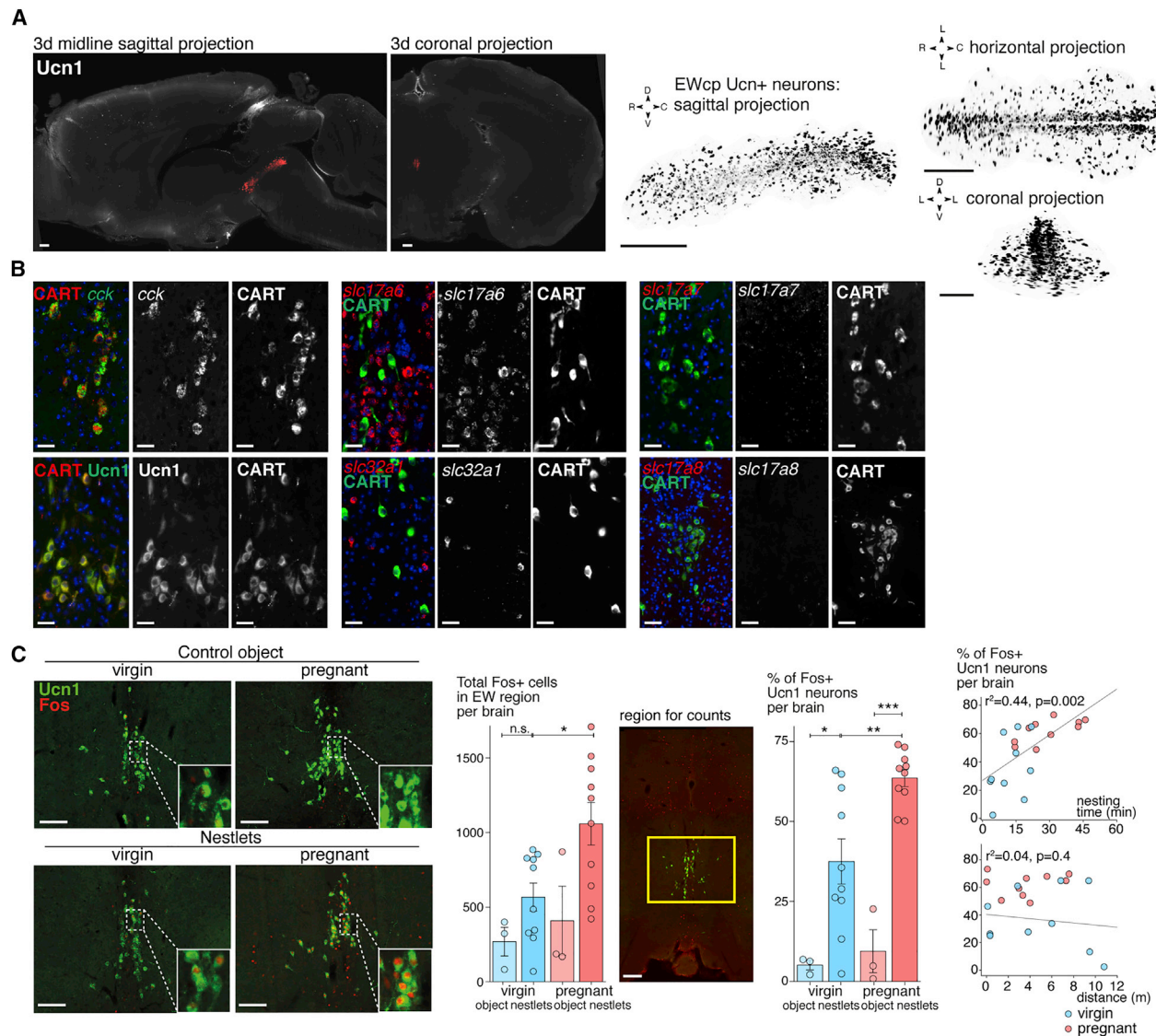
**Figure 3. Nesting activates the peptidergic neurons of the Edinger-Westphal in virgin and pregnant mice**

(A) Whole-brain iDISCO+ immunolabeling for Ucn1, with the EW nucleus highlighted in red. Volumes extracted of the EW locus show the distribution of Ucn1+ neurons along the rostro-caudal axis.

(B) Sections at the level of the EWcp nucleus, immunolabeled for Ucn1 and CART, and hybridized for *cck*, *slc32a1* (vGat), *slc17a6* (vGlut2), *slc17a7* (vGlut1), *slc17a8* (vGlut3), or *cartpt* (CART). Ucn1+ neurons of the EWcp nucleus co-express CART and CCK but no markers of fast neurotransmission (vGlut2 or vGat).

(C) Ucn1 and Fos immunolabeling in virgin and pregnant controls or nest builders. Fos expression is significantly increased in the EW region in pregnant nest builders (the area used for counting is indicated in the yellow square). Fos co-localization is significantly increased specifically in Ucn1+ neurons during nesting in pregnant nest builders, as well as in virgin nest builders but to a lesser extent. Scale bars are 250 (A), 50 (B), and 150 μm (C). * P < 0.05, ** P < 0.01, *** P < 0.001. All data are presented as mean ± SEM. Unpaired Mann-Whitney ranked U test (C, middle panels) and Wald's test with t-distribution (C, right panels). See also Video S2.

pontine formation and the EW nucleus (Figure 2E). We reasoned that the increased activity located in the pontine gray might correlate to the elevated motor activity during nesting and focused our attention on the EW.

**Peptidergic signaling by EW neurons is necessary for high nest scores in virgin and pregnant mice**

The increase in Fos expression in the EW was significant across most of the rostro-caudal extent in pregnant and pseudopreg-

nant nest builders (Figure 2E). We confirmed by 3D iDISCO+ immunolabeling for Ucn1 and CART that the distribution of EWcp neurons matched the p value of nesting-induced voxels noted in the ClearMap analysis (Figures 3A and S2B; Video S2). We aimed to identify the composition of the EWcp by using fluorescent *in situ* hybridization combined with immunohistochemistry.

We determined that the EWcp nucleus contains at least three non-overlapping neuronal populations: vGlut2+ (*slc17a6*) glutamatergic neurons, vGat+ (*slc32a1*) GABAergic neurons,
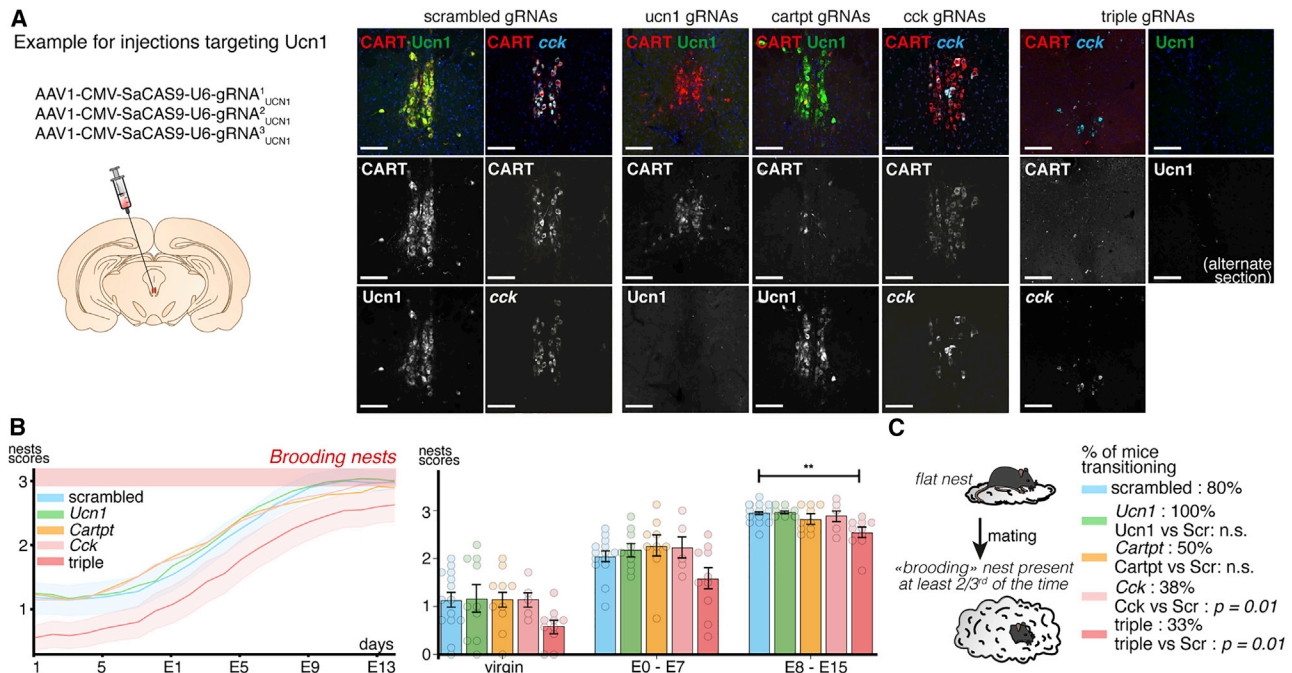
**Figure 4. CCK signaling by Edinger-Westphal neurons is necessary for the switch to preparatory nesting during pregnancy**

(A) Sections at the level of the EW nucleus in animals injected in the EW with 3 AAVs expressing saCas9 and one of 3 gRNAs targeting Ucn1, CART, or CCK expression, showing the specific deletion of each gene (an example of the constructs injected is shown for Ucn1). CART and Ucn1 gRNAs lead to almost complete loss of expression, but mice injected with CCK gRNAs still retain some expression. The efficiency of deletions is similar in the triple knockdowns and in the single knockdowns.

(B) Rolling-average nest scores of these animals. Only the triple knockdown has significantly reduced scores.

(C) Proportion of mice transitioning to preparatory nesting in the cohort. CART and CCK knockdowns reduce the proportion of mice consistently building preparatory nests. Scale bars are 150 μm. ** P < 0.01. All data are presented as mean ± SEM. Dunn's multiple comparisons test (B) and unpaired Mann-Whitney ranked U test (C). See also Figure S3.

and peptidergic neurons co-expressing CART, CCK, and Ucn1 (100% of overlap between these markers in the EWcp, n = 4,984 cells counted) and no markers of fast neurotransmission: 0% of overlap between CCK and vGlut2 in the EWcp (n = 3; 1,268 cells counted). No expression of vGlut1 nor vGlut3 was detected in the region (Figure 3B).

We evaluated which of these three populations were driving the increase in Fos expression in the EWcp of pregnant nest builders on brain sections. A significant increase in Fos+ cells was detected in the EW region only in pregnant nest builders (all cell types), consistent with the ClearMap region-level and 3D voxel data (Figures 2D, 2E, and 3C). While nest building induced a significant increase in the proportion of Ucn1+ neurons expressing Fos in both virgin and pregnant females (Figure 3C), pregnant females had a significantly higher proportion of co-localization (62% ± 3% versus 37% ± 7%, p = 0.007, n = 11/10 mice/group). The proportion of Fos-expressing Ucn1+ neurons was also correlated with the time spent nesting but not general locomotor activity (Figure 3C). These data suggest that the peptidergic neurons of the EWcp are always recruited during nest building but significantly more during pregnancy, while suggesting that other populations in the region may also respond to nesting.

We next tested which EWcp neuropeptide was involved in regulating nesting during pregnancy. We injected in the EWcp

nucleus of wild-type C57BL/6NRj mice AAVs expressing saCas9 and one of three guide RNAs targeting either *Ucn1*, *Cartpt*, or *Cck*. We validated the knockdowns by immunolabeling and *in situ* hybridization on sections (Figures 4A and S3A). The Ucn1 knockdown was complete. In the CART+ knockdown, only a very few CART+ neurons remained (n = 1.7 ± 0.4 versus 22.4 ± 2.7 neurons/slice). In the *Cck* knockdown, 48% of Ucn1+ neurons still expressed *Cck* (n = 2; 1,089 cells counted). As a small group of CCK+ neurons exists ventral to the EW belonging to the rostral linear raphe, it is likely that CCK expression was also perturbed in these neurons (Figure S3A). We noted comparable efficacies for the three genes in the combined triple knockdown (Figure 4A). None of the single knockdowns showed a significant reduction in average nesting scores compared with the scrambled controls at the cohort level. However, we observed a significant reduction in nesting scores in the triple knockdown only in the second week of pregnancy (2.6 ± 0.1 versus 3.0 ± 0.1, p = 0.007) (Figure 4B). We then counted the proportion of mice transitioning to building preparatory nests consistently in their second gestational week. Then, 80% of the scrambled controls had transitioned to preparatory nests. While these proportions were not significantly different in Ucn1 and CART knockdowns compared with controls (p = 0.08 and p = 0.07, respectively), they fell to 38% for the CCK and 33% for the triple knockdowns (Figure 4C, p = 0.01 and p = 0.01,

respectively, when compared with scrambled controls). These results suggest that the action of the EWcp neurons on preparatory nesting likely involves the combined secretion of several neuropeptides with CCK likely playing a major role, consistent with other observations that its receptor CCKAR could be involved in regulating parental nesting (Maynard et al., 2018; Xu et al., 2012).

### Peptidergic neurons of the EW are required for preparatory nesting during pregnancy

In order to identify whether peptidergic neurons of the EWcp are necessary for the mice to build preparatory nests during pregnancy, we conducted specific ablation studies using the *Cart-Cre* driver line. We verified that this line enables a specific targeting of the EWcp peptidergic neurons (Figures S3B–S3E). To ablate these neurons, we injected a Cre-dependent AAV expressing an activated caspase 3 (Yang et al., 2013) in hemizygous *Cart-Cre* females and Cre-negative littermate controls. Two weeks after the injection, we counted a substantial reduction in the number of CART+ neurons throughout the rostro-caudal axis (Figures 5A and S3E) (128 ± 14 versus 1,161 ± 43, p = 0.016, n = 5/4 mice/group). The total number of neurons in the EW region by NeuN expression (a general marker of neurons) was not affected by the construct (302 ± 4 versus 302 ± 12 neurons/slice, n = 2/3 control/Cart-Cre, 5,983 ± 21 NeuN+ cells counted per brain) (Figure S3G). The ablation decreased the baseline nest scores in virgin over control mice (1.0 ± 0.2 versus 1.3 ± 0.2, p = 0.04, n = 10 mice/group) and only showed minor improvement of nest quality during pregnancy (2.1 ± 0.2 versus 3.0 ± 0.1, p = 0.002, n = 10/9) (Figure 5B). In the lesioned group, this decrease in nesting scores led to a stark reduction in the frequency of preparatory nests, as only 10% of the mice transitioned to building a brooding nest during pregnancy, versus 78% in the control group (p = 0.002) (Figure 5B).

We next assessed whether the loss of EWcp$^{CART+}$ neurons affects nesting sequences. We designed a video tracking system to automatically segment bouts of nesting activity and rest, based on the live mouse tracker design (Chaumont et al., 2019) (Figures 5C and S4; Video S3). While the "nestlet interaction" segmentation is more inclusive than "nest building," very few interactions occur outside of nesting phases. Virgin control and EWcp$^{CART+}$-lesioned females performed similarly throughout the day, with their cumulative nesting curves overlapping (nestlet interaction time over 5 h: 10.0 ± 4.8 min versus 12.0 ± 3.6 min, p = 0.6, n = 8/6 mice/group) and with a comparable number of switches toward nesting from other behaviors (39 ± 10 versus 48 ± 17, p = 0.9) (Figure 5D). However, at 2 weeks of pregnancy, the cumulative nesting curves markedly diverged between the groups (Figure 5E). EWcp$^{CART+}$ neuron ablation led to a decrease in the overall nesting time (7.8 ± 3.3 min versus 30.5 ± 7.5 min, p = 0.032, n = 5 mice/group) and in the number of behavioral switches toward nesting (20 ± 5 versus 63 ± 9, p = 0.008) (Figure 5E).

To test whether there was a general defect in the capacity to build complex nests rather than a specific defect in preparatory nesting, we tracked parental nesting in the presence of the offspring. In the presence of pups, control and ablated females exhibited similar nesting behaviors (total nesting time over 1 h: 10.2 ± 3.5 min versus 12.9 ± 2.5 min, p = 0.4, nesting initiation

delay: 3.4 ± 0.5 min versus 2.8 ± 0.9 min, p = 0.84, n = 5 mice/group) (Figure 5F). Therefore, the lack of EWcp$^{CART+}$ neurons does not affect the nesting response induced by external cues such as pups.

Ablation of EWcp$^{CART+}$ neurons could have long-lasting consequences on homeostatic regulations, such as sleep and body temperature, that could indirectly affect nesting/sleep transitions. We measured sleep patterns, core body temperature, and food intake in ablated animals. Sleep intervals over 3 days were unaffected (Figure S5A). Daily core body temperature oscillations were also normal in ablated animals in virgin and pregnant states (Figure S5B). Food intake remained surprisingly unaltered between groups (Figure S5C), as it is known that EWcp$^{CART+}$ neurons are leptin sensitive and integrate stress response with feeding (Xu et al., 2011, 2014). Our results expand those findings, showing that these neurons may not be necessary for the control of food intake in baseline conditions. We therefore also tested anxiety (amount of time spent in the open arms of an elevated plus maze), which remained unaltered between control and ablated groups (Figure S5D). General maternal behaviors, measured as the latency to retrieve pups to the nest, were not affected (Figure S5E).

### Peptidergic EW neuron activation precedes nesting and controls behavioral transitions to nesting

To determine whether the activity of EWcp$^{CART+}$ neurons has a direct influence on nesting in the wake-to-sleep sequence during pregnancy, we recorded their calcium activity *in vivo* via fiber photometry (Dana et al., 2019) (Figure 6A). EWcp$^{CART+}$ neurons had low and stable calcium fluorescence during sleep, except for regularly spaced peaks of signals correlated with muscular twitches (Figures 6B and S6A). Conversely, the calcium-dependent signal was generally high during aroused periods (Figure 6B). Peri-event plots of activity synced to specific behavioral onsets showed a sharp increase during awakening and a fast decrease when the animal falls asleep (Figure 6C). Intriguingly, EWcp$^{CART+}$ neurons exhibited a slow rise in activity during nesting, starting at around 10 to 15 s before nesting onset (Figure 6C). Digging also correlated with stronger calcium transients (Figure S6A). Overall, the activity levels of EWcp$^{CART+}$ neurons recorded were synchronized with the wake-to-sleep behavioral sequence: activity increased at the beginning of the sequence during nesting and dropped sharply at the onset of sleep (Figures 6B and 6C).

To test whether EWcp$^{CART+}$ neurons bidirectionally modulate preparatory nesting, we used chemogenetic and optogenetic approaches. We first tested whether inhibition of the EWcp$^{CART+}$ neurons at the beginning of the light phase disrupts the nesting sequences. To do so, we used chemogenetic inhibition, injecting a Cre-dependent AAV expressing the inhibitory DREAADs tagged with mCherry (Krashes et al., 2011) in the EW nucleus of *Cart-Cre* females. We used littermate Cart-Cre females injected with a mCherry expressing AAV as controls. Females were mated 7 days later, and nesting behavior was evaluated during the light phase at E14 and E15 following intra-peritoneal (IP) injections of CNO and saline (Figure 6D). CNO injections reduced nestlet interaction time compared with saline in pregnant mice injected with the inhibitory DREAADS (9.2 ± 3.3 min
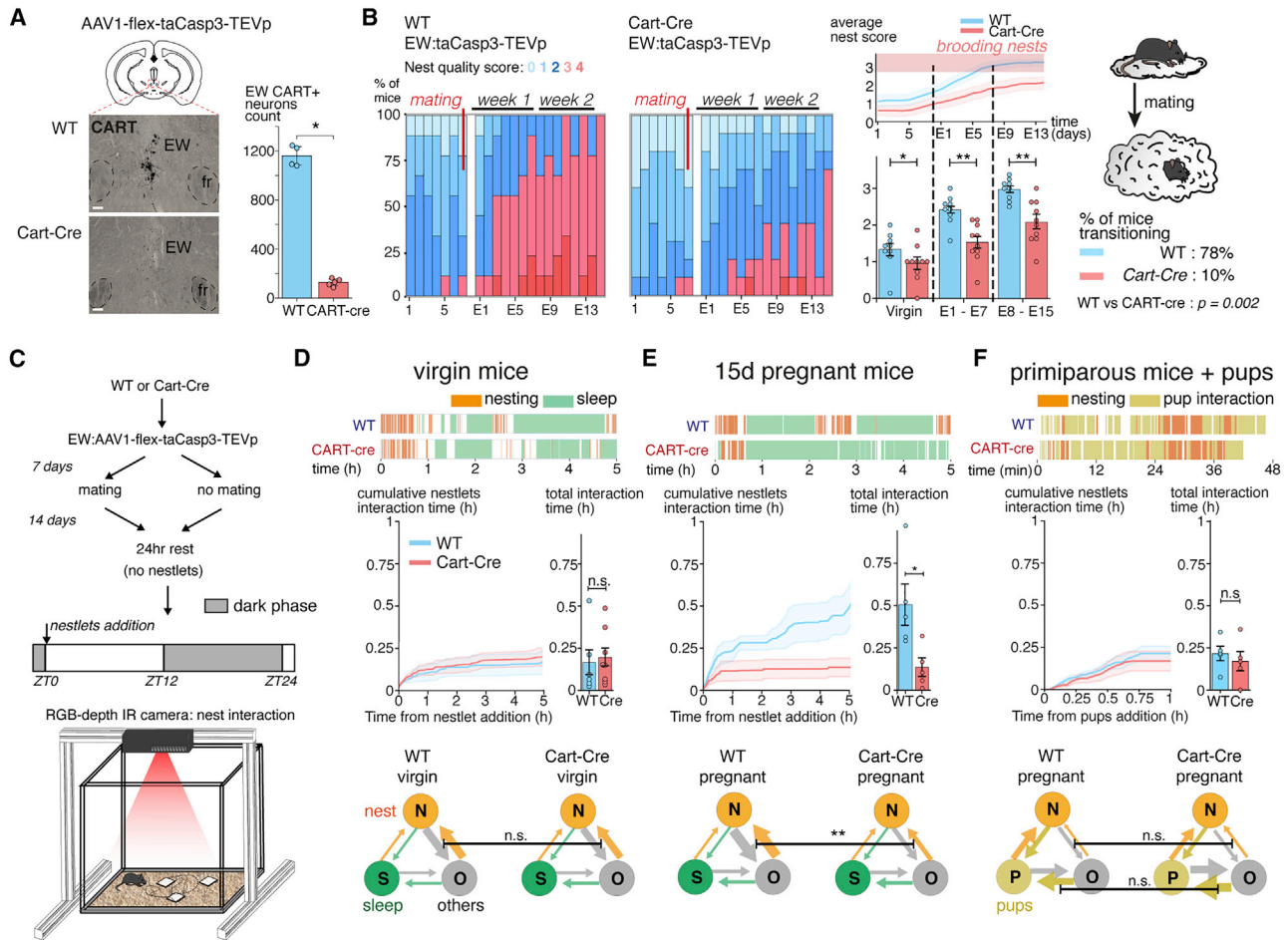
**Figure 5. Peptidergic neurons of the EW nucleus are required for preparatory nesting during pregnancy**

(A) CART+ neurons specific lesion: brain sections immunolabeled for CART at different levels of the EWcp nucleus following an injection of an AAV1 virus carrying a loxed endogenously activated taCasp3-TEVp construct. The number of CART+ neurons is strongly reduced in CART-cre animals compared with injected WT controls.

(B) Proportion of brooding nests (left panels) in a cohort of WT or CART-cre mice lesioned for the EWcp$^{CART+}$ neurons and evolution of the nest scores after mating (right panel). After mating, only 10% of lesioned animals build brooding nests reliably (more than 2/3$^{rd}$ of the time), compared with 78% of the unlesioned control animals. The nest scores of lesioned animals are lower in virgins and throughout pregnancy.

(C) Automated video tracking of nestlets interactions in WT or CART-cre animals injected with taCasp3-TEVp over 5 h.

(D) In virgin females, the cumulative curves of nestlets interactions in control and lesioned animals overlap and behavior switches are similar.

(E) In pregnant control females, the cumulative time interacting with nestlets increases compared with virgin controls but not in lesioned females. Behavior switches throughout the session: the weight of the arrows is proportional to the number of times the mouse switches between two behaviors. In pregnant lesioned mice, the alternation between nesting and general activity is reduced compared with pregnant controls.

(F) In primiparous mice exposed to pups, the nestlets interaction time is high in both control and lesioned mice (measured over 1 h). The ablation in Cart-Cre mice doesn't affect the transitions towards nesting in the presence of pups. Scale bars are 150 μm. * P < 0.05 and ** P < 0.01. All data are presented as mean ± SEM. Unpaired Mann-Whitney ranked U test (A, B, and D-F). See also Figures S3–S5 and Video S3.

---

CNO versus 33.7 ± 11.8 min saline, p = 0.008, n = 8 mice), unlike in mCherry-injected animals (37.0 ± 5.0 min CNO versus 37.1 ± 5.8 min saline, p = 1.0, n = 9 mice) (Figures 6E and 6F). Moreover, sleep time was significantly increased over the 5 h course of the experiment in the inhibitory DREAADS-injected group (214.4 ± 13.1 min CNO versus 172.9 ± 8.9 min saline, p = 0.02) but not in the control mCherry-injected animals (165.9 ± 9.1 min CNO versus 164.8 ± 6.2 min saline, p = 0.92). Behavioral transitions from exploration to nesting were reduced in the CNO-injected animals (Figure 6G). Grooming, eating, drinking times, and loco-

motor activity were not affected by the chemogenetic inhibition of EWcp$^{CART+}$ neurons (Figure S6B).

We next tested whether activating the EWcp$^{CART+}$ neurons via optogenetic stimulation could promote nesting. We co-expressed the calcium indicator jGCaMP7s with the ChrimsonR opsin (Klapoetke et al., 2014) in EWcp$^{CART+}$ neurons, allowing us to monitor the calcium transients induced by the stimulation, with control mice receiving only the jGCaMP7s-expressing virus (Figure 6H). Stimulations of 30 s at 20 Hz correlated with a switch to nesting in virgin awake mice injected with ChrimsonR in

(legend on next page)

**Neuron**
Article

**CellPress**
OPEN ACCESS
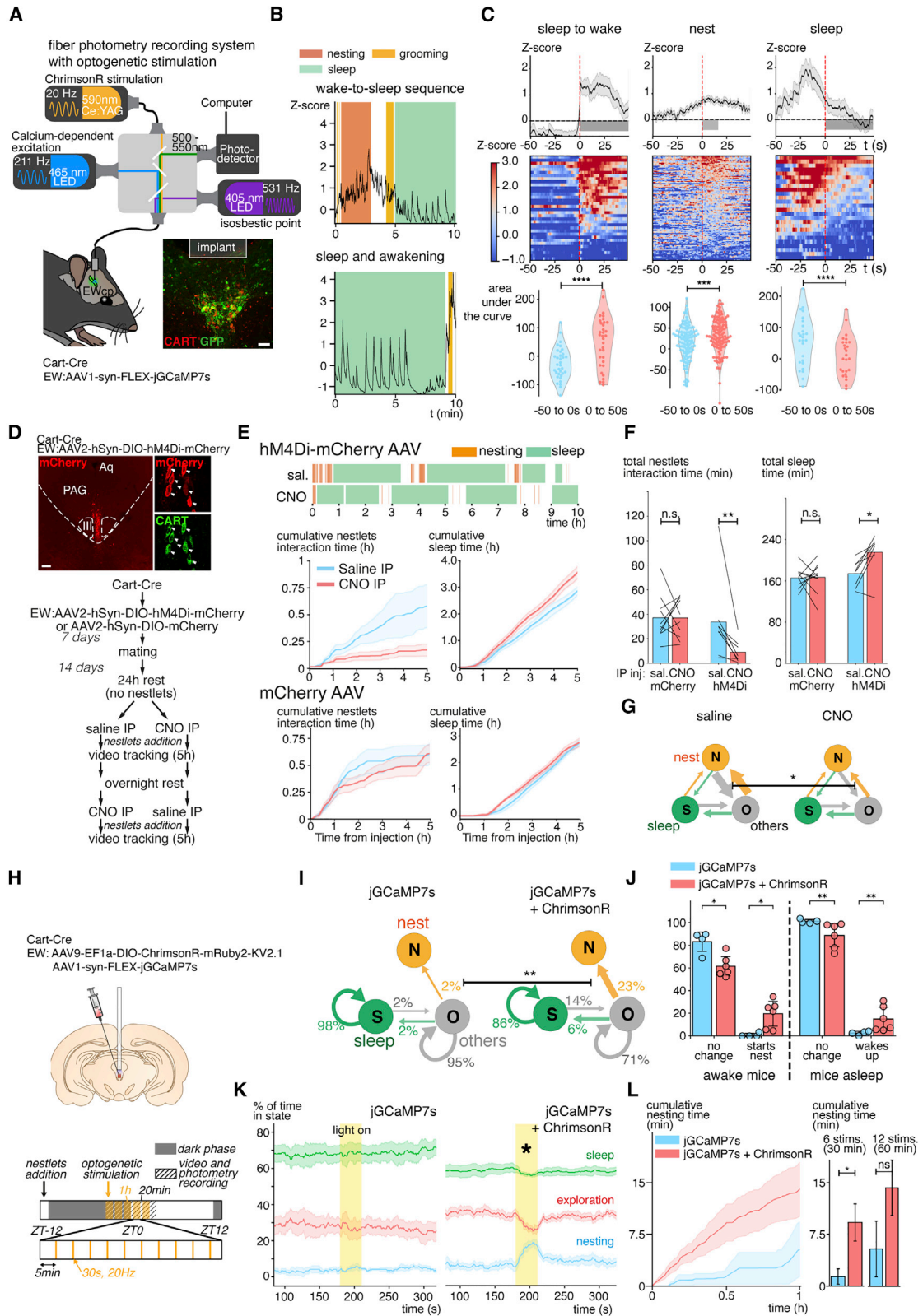
19.6% ± 4.9% of the stimulations versus 0.9% ± 0.9% in control animals (n = 6/4 mice/group, p = 0.01) (Figures 6I and 6J). Then, 14.4% ± 4.4% of the stimulations triggered during sleep correlated with awakening in the opsin-injected animals (versus 2.4% ± 0.9% in controls, p = 0.01). The stimulations significantly changed the probability of the mouse to perform nesting over exploration (Figure 6K) but did not trigger switches to other behaviors (Figure S6C). A significant increase in the cumulative nesting time over controls could be observed for the first few sequences of stimulations but not during the second half of the stimulation period (Figure 6D). Activating the neurons with excitatory DREADDs hM3Dq did not modulate nesting nor sleep time in virgin mice over an extended time, suggesting that longer or continuous bouts of stimulations of EWcp$^{CART+}$ neurons with optogenetics or chemogenetics are not effective in modulating nesting (Figure S6E). Altogether, optogenetic stimulations, calcium recordings, and chemogenetic inhibition data demonstrate that the activity of EWcp$^{CART+}$ neurons is fundamental in the control of nesting initiation.

### Peptidergic EW neuron properties are modulated by progesterone and are required for the action of progesterone on preparatory nesting

We next turned to the impact of the pregnancy hormone progesterone on EWcp$^{CART+}$ neurons and preparatory nesting. We prepared subcutaneous progesterone implants (5–25 mg) and tested their impact on circulating progesterone by measuring its serum concentration by ELISA (Figures S7A and S7B). Of note, the physiological progesterone levels were similar between EWcp$^{CART+}$ ablated and control females before and during pregnancy (28.8 ± 1.0 versus 25.4 ± 1.9 ng/mL at E15, p = 0.19, n = 5/4 mice) (Figure S7B). The circulating progesterone concentrations measured after implantation were sufficient to trigger a behavioral switch to preparatory nesting 4–6 days after implantation, with 71% of mice switching to building preparatory nests 2 weeks after implantation (Figures 7A–7C and S7C). To test the role of EWcp CART neurons, we compared the effect of progesterone implants on nesting in control and EWcp-lesioned mice. Ablated females were less responsive to progesterone implants than controls (nest scores: 1.6 ± 0.5 versus 2.9 ± 0.4, p = 0.04, n = 9/7 mice) (Figures 7A–7C). As during normal pregnancies, progesterone implants triggered a shift in the circadian fluctuation of core body temperature in both groups (Figure S7D). EWcp$^{CART+}$ neurons are therefore necessary for the action of progesterone on the modulation of the behavioral sequence enabling preparatory nesting but not for its effects on core body temperature.

We explored whether progesterone modulates the activity of these neurons. We performed visually guided slice patch-clamp recordings of CART+ neurons in the EWcp nucleus after Cre-dependent eYFP AAV injections in *Cart-Cre* mice. EWcp$^{CART+}$ neurons are tonically active at resting membrane potential with a frequency of 5.1 ± 0.7 Hz (n = 16 cells, 8 mice) and receive strong excitatory synaptic currents (Figure 7D). Comparisons between recordings of virgin and pregnant female mice showed no changes in intrinsic passive properties, threshold excitability, and synaptic activity (Figures S8A and S8B). Intra-cellular injections of depolarizing current pulses revealed different firing responses classified into 3 categories, expanding on previous findings obtained from juvenile rats (Laursen and Rekling, 2006): (1) repetitive regular firing neurons whose frequency linearly increases with the injected current (46%), (2) transient firing neurons with an intense burst of action potential at the beginning of the pulse (18%), and (3) irregular firing neurons that combined both the initial burst followed by irregular firing (36%) (Figures 7E and S8C). The firing mode of the neurons did not strongly affect the strength of the calcium transients imaged with the jGCaMP7s reporter (Figure S8D); therefore, changes in the firing mode of the neurons may not account for the increased calcium signal recorded during nesting *in vivo* (Figure 6C).

We evaluated whether progesterone affects these firing patterns. Progesterone can act either on a nuclear receptor (PGR) or on a membrane receptor (mPR) (Kapur and Joshi, 2021). While we could not detect PGR expression in the EW

---

**Figure 6. Peptidergic EW neuron activation precedes nesting and controls behavioral transitions to nesting**

(A) Fiber photometry recording of EWcp neurons calcium activity with GCaMP7s.

(B) Motion-corrected (isosbestic point) calcium-dependent fluorescence over a full sequence of behavior, with zooms at the level of the waking, nesting, and sleep transitions in virgin females. Two different modes of activity are visible, during wakefulness and during sleep.

(C) Peri-event plots of awakening, nesting, and sleep transitions in virgin females. Activity of the EWcp$^{CART+}$ neurons peaks after the animal wakes up and rises before nesting onset and falls at sleep onset.

(D) Acute inhibition of EWcp$^{CART+}$ neurons with hM4Di in Cart-Cre mice.

(E) Cumulative nestlets interaction time in E14–E15 pregnant females injected with an AAV2 expressing hM4Di or mCherry, following saline or CNO IP injections over 5 h. CNO-injected females spend less time nesting and more time sleeping than saline injected mice for the hM4Di injected group only.

(F) Pairwise comparisons of total nesting and sleep times in mice injected with the control or hM4Di virus, following saline and CNO injections.

(G) Behavioral transitions following saline or CNO injections in hM4Di-injected pregnant females, with a significant reduction in switches toward nesting.

(H) Regimen of acute stimulations of the EWcp$^{CART+}$ neurons with ChrimsonR in virgin Cart-Cre females: five sessions of 1 h are distributed around the switch from the dark to the light phase. During each 1-h session, trains of 20-Hz stimulations for 30 s are initiated every 5 min.

(I) Proportion of stimulations in virgin females that elicit a switch in behavior. Stimulations randomly occur during either sleep or active behaviors, and the ratio of stimulation leading to a switch over ineffective stimulations is evaluated.

(J) Switches of behavior evoked by the stimulation in control and opsin-injected virgin female mice. Random stimulations evoked a switch toward nesting in 23% of the time in awake animals.

(K) Behavioral state of the animals around stimulations, showing an increase in the proportion of time spent nesting in ChrimsonR-injected animals during the stimulation.

(L) Cumulative time spent nesting in control and ChrimsonR-injected animals over the 1 h of stimulations, as in (H). The stimulated animals spend more time nesting but only during the first half of the stimulation periods. Scale bars are 50 (A) and 150 μm (D). * P < 0.05, ** P < 0.01, *** P < 0.001, and **** P < 0.0001. All data are presented as mean ± SEM. Wilcoxon's signed rank test (C, F, and K) and unpaired Mann-Whitney ranked U test (G, I, J, and L). See also Figure S6.
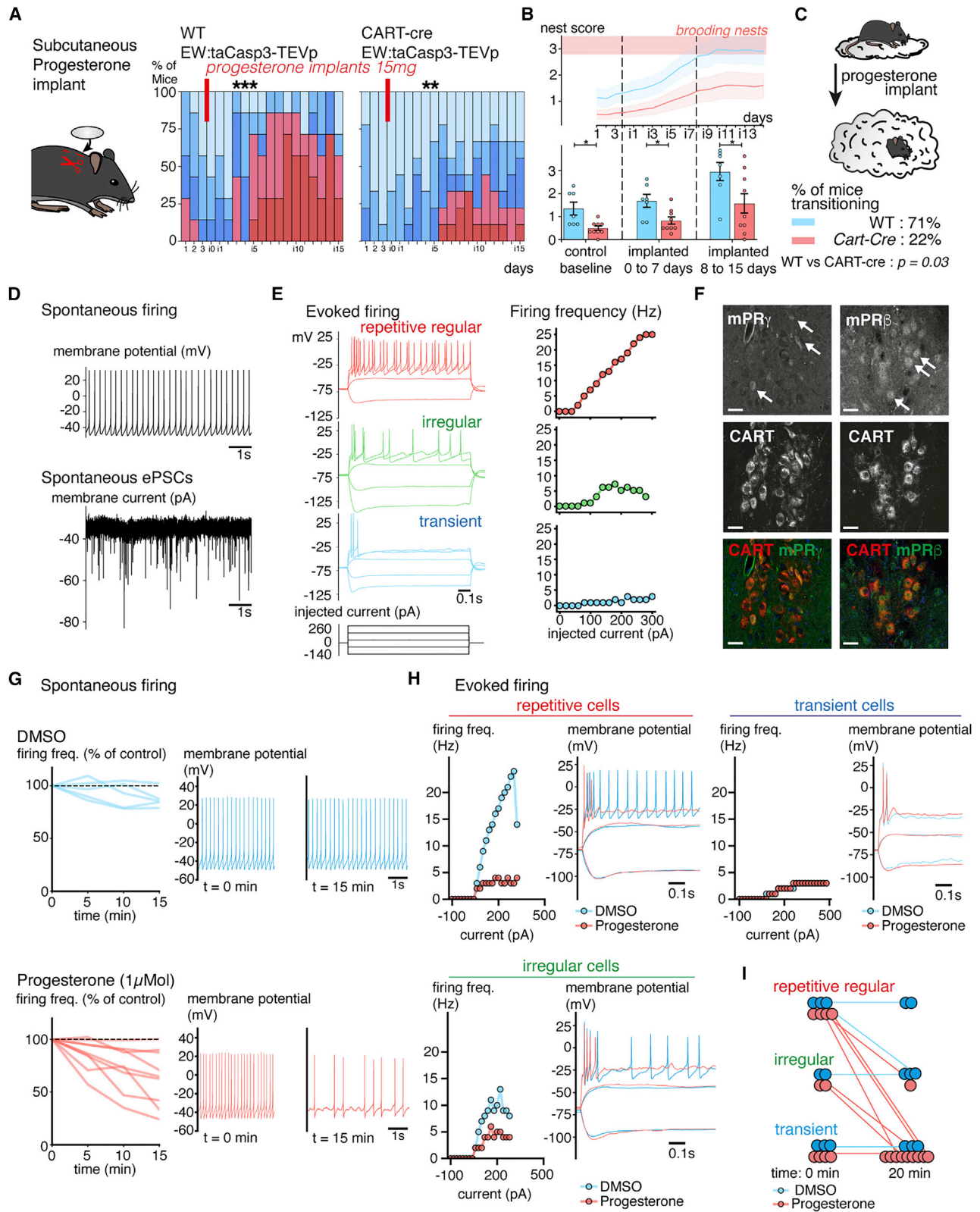
*(legend on next page)*

via immunohistochemistry (Figure S8E), mPR-beta and mPR-gamma receptors were detected in 52% ± 2% and 56% ± 2% of CART+ neurons, respectively (Figure 7F). Acute bath application of 1 µMol of progesterone reduced the spontaneous firing frequency at resting membrane potential in 6 out 9 recorded neurons within 15 min (Figure 7G). The presence of progesterone in the bath could also convert the evoked firing pattern of repetitive regular and irregular neurons into transient bursting neurons (Figures 7H and 7I). The timing of this effect suggests a metabotropic action of progesterone on the EWcp$^{CART+}$ neurons.

### EW neurons modulate a broad network of downstream arousal and nesting centers in the brain

To evaluate the downstream network of these neurons and assess which regions can be modulated by EWcp$^{CART+}$ neurons, we generated whole-brain projection maps from stereotaxic injections of an AAV2-Ef1a-DIO-eYFP virus in *Cart-Cre* females. The brains were cleared (iDISCO+) and scanned at a 5-µm resolution using a light sheet microscope (Figure 8A; Video S4). We mapped throughout the brain the location of EWcp$^{CART+}$ projections using a combination of TubeMap and TrailMap (Friedmann et al., 2020; Kirst et al., 2020) (Figures 8B and 8C). We found high densities of projections in the brainstem, midbrain, hypothalamus, amygdala, and prefrontal cortex (Figures 8C and 8D), with the highest density recorded in the supraoptic nucleus (Figure 8D).

To evaluate which projection sites are functionally activated, we mapped Fos induction throughout the brain after activating these neurons with the excitatory DREADD hM3Dq in pregnant females (Figure 8E). CNO injection in hM3Dq expressing *Cart-Cre* females induced a strong Fos expression in EWcp neurons (Figures 8F and 8G) and many other brain regions (Figures 8G and 8J). To find the regions whose activity was changed by both preparatory nesting and chemogenetic activations of EWcp$^{CART+}$ neurons, while also receiving dense projections from them, we combined three whole-brain mapping datasets (Figures 8H and 8I): Fos expression elicited by nesting over control objects, elicited by CNO in HM3Dq over controls, and EWcp$^{CART+}$ projections.

The overlap between these datasets showed a distributed array of nuclei among which the preoptic area and suprachiasmatic nuclei, the zona incerta, the central, basolateral, and basomedial amygdala, the ventrolateral periaqueductal gray, and the brainstem reticular formation (Figure 8J). These regions are known to be involved in sleep, arousal, parental behaviors, and general nesting. Many of these regions identified here were also present in the initial screen of regions activated in all nest builder groups (including males).

The nature of the potential EWcp target regions identified through this screen suggests a broad modulation of regions controlling nesting and arousal.

### DISCUSSION

The neuronal mechanisms controlling preparatory nesting during pregnancy have remained largely unexplored. Starting from an unbiased whole-brain survey of activity patterns elicited in different contexts, we associate a group of midbrain neurons, the EWcp$^{CART+}$, with maternal behavior. Of note, nesting is most often performed as the first step of a behavioral sequence that leads the animal to sleep (Eban-Rothschild et al., 2016; Sotelo, 2022). Our data suggest that the activity of the EWcp$^{CART+}$ neurons acutely influences the transition to nesting in the wake-to-sleep sequence, and their inhibition is detrimental to the duration of the nesting phase in the sequence. It also suggests that the long nesting bouts necessary for preparatory nesting occur at the expense of sleep. This is reminiscent of a role recently described for VTA dopaminergic neurons in regular nesting (Eban-Rothschild et al., 2016), which have been suggested to interact with EWcp neurons functionally (Ryabinin et al., 2013). Intriguingly, loss-of-function or silencing experiments show that EWcp$^{CART+}$ neurons have a more significant impact on the nesting sequence in pregnant mice than in virgins by increasing the time allotted to nesting during pregnancy. It is possible that during pregnancy, the sequence deviates from its homeostatic set point and that EWcp$^{CART+}$ neurons are essential in establishing a novel set point in pregnant females under hormonal control.

---

**Figure 7. Peptidergic EW neuron properties are modulated by progesterone and are required for the action of progesterone on preparatory nesting**

(A) Progesterone implantation in virgin mice. Subcutaneous implantation of progesterone triggers the onset of preparatory nesting by itself. The effect of the implants on preparatory nesting is blunted in Cart-Cre lesioned mice compared with WT controls.

(B) Quantification of nests scores following implantation in WT controls and Cart-Cre lesioned mice. Nest scores are significantly reduced in lesioned mice over controls.

(C) Only 22% of lesioned mice transition to preparatory nesting 2 weeks after implantation instead of 71% of control mice.

(D) Patch recording in acute slices of the EWcp$^{CART+}$ neurons in Cart-Cre mice injected with an AAV1-DIO-eYFP virus to visually guide the patch pipette (D–I). Spontaneous tonic firing and excitatory postsynaptic currents (spontaneous EPSC) at resting membrane potential and −70 mV respectively.

(E) Evoked firing at the −70 mV holding potential reveals 3 types of responses in the CART+ population: repetitive regular firing, irregular firing, and transient bursting neurons.

(F) Section at the level of the EW nucleus immunolabeled for CART and mPRβ or mPRγ, showing expression of membrane progesterone receptors in some CART neurons (arrows).

(G) Firing frequency at resting membrane potential of EWcp$^{CART+}$ neurons, showing a decrease of the spontaneous firing rate 15 min after the application of progesterone at 1 µM. Frequency changes are represented in % of control measured at the onset of the recording in control condition (DMSO) or at the time of drug application.

(H) Conversion of the evoked firing, 20 min following the application of progesterone, from repetitive or irregular to bursting firing.

(I) Summary of the evoked firing conversions observed for all recorded cells.

Scale bars are 50 µm. * $P < 0.05$, ** $P < 0.01$, and *** $P < 0.001$. All data are presented as mean ± SEM. Wilcoxon's signed rank test (A) and unpaired Mann-Whitney ranked U test (B and C). See also Figures S7 and S8.
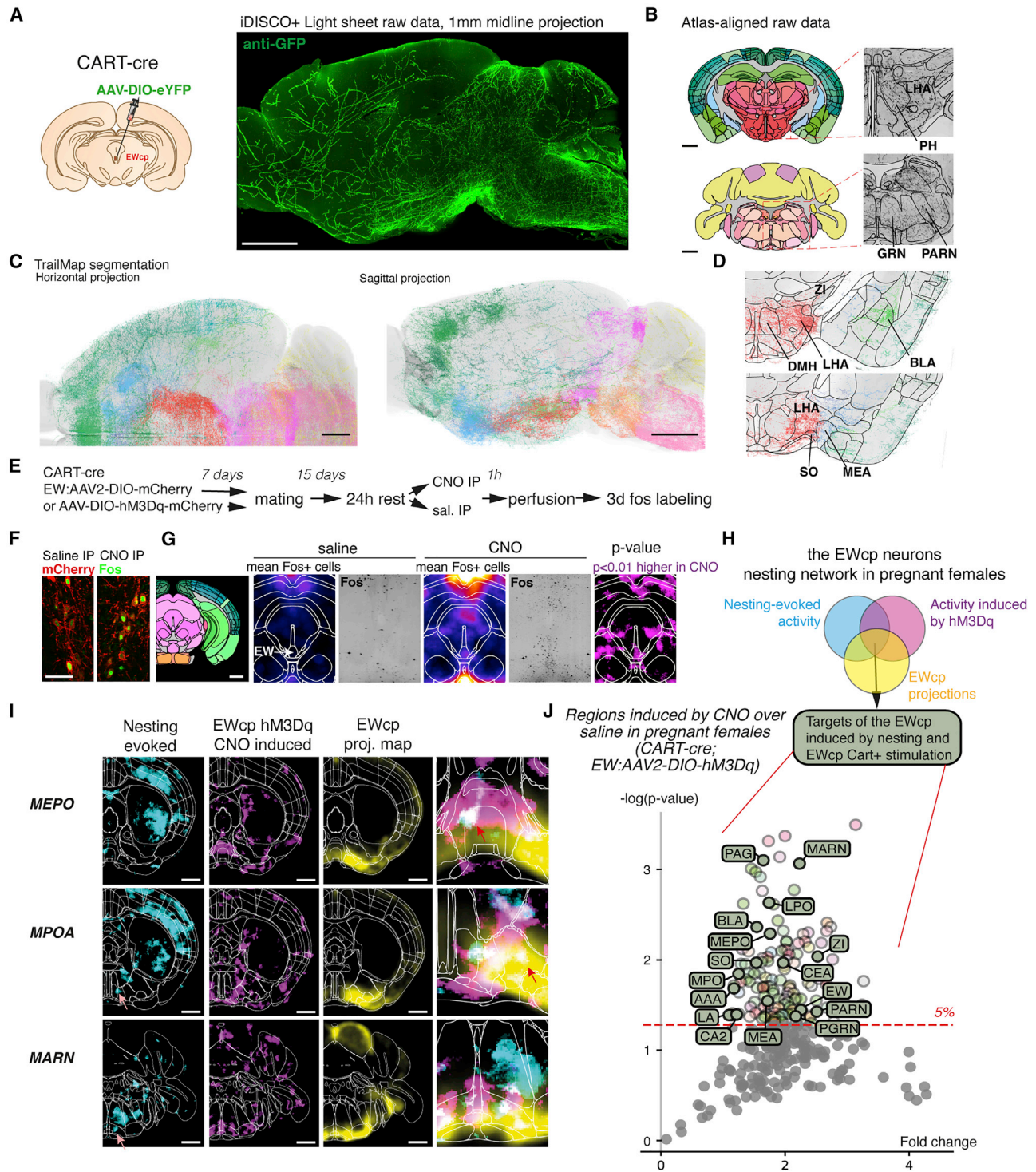
**Figure 8. Peptidergic neurons of the EWcp enable preparatory nesting through the modulation of a broad network of downstream arousal and nesting centers in the brain**

(A) Whole brain mapping of labeled EWcp[CART+] projections with iDISCO+ clearing. Sagittal projection of the light sheet data is shown.

(B) Atlas-aligned raw data (coronal projections).

(C) Segmented projections of EWcp[CART+] neurons using TrailMap and ClearMap, showing dense projections in the brainstem and hypothalamus.

(D) Coronal section of the segmented data highlighting regions of dense projections.

(E) Strategy to map the brain-wide activation pattern elicited by the stimulation of EWcp[CART+] neurons in hM3Dq- or mCherry-injected pregnant mice.

*(legend continued on next page)*

# Neuron
## Article

**CellPress**
OPEN ACCESS

The number of urocortin1-expressing neurons in this nucleus has been correlated, in different vole species, with parental investment strategies (Lim et al., 2006), which could be incidental to their role in promoting maternal nesting during pregnancy. Considering the projection patterns of these neurons (Figure 6; Dos Santos Júnior et al., 2015; Silva et al., 2013), it would therefore be interesting to test further how the action of EWcp$^{CART+}$ neurons integrates with other structures controlling social behaviors, such as the lateral septum, the preoptic areas, the VTA, and the dorsal raphe nucleus.

We confirmed that progesterone alone in the mouse replicates the effects of pregnancy on nest building (Figure 5A; Lisk et al., 1969) and core body temperature regulation (Figure S5D). Membrane progesterone receptors belong to either a family of 5 protein G-coupled transmembrane receptors (mPR alpha through epsilon) or cytochrome-$b_5$-related receptors PGRMC1 and PGRMC2. mPRs modulate metabotropic channels in neurons through the action of progesterone or its brain metabolite allopregnanolone (Kapur and Joshi, 2021). While the neuroactive derivative of progesterone, allopregnanolone, is thought to have a broad neuromodulatory effect by acting through GABA receptors (Parakala et al., 2019), documented cases of a direct action of progesterone on neurons outside of its transcriptional effects have been primarily investigated in hypothalamic neurons, such as GnRH neurons (Bashour and Wray, 2012; Kapur and Joshi, 2021). We show that the EWcp$^{CART+}$ neurons are also hormone sensitive to acute applications of progesterone, likely signaling through its membrane receptors given its fast action. The mapping of potential EWcp$^{CART+}$ targets (Figure 7) suggests that these neurons' control of preparatory nesting occurs through a diffuse brain-wide network of regions rather than a linear chain of downstream targets, and thus, it could transfer the hormonal signals they receive broadly by modulating distant target regions.

Finally, EWcp neurons belong to an ancestral arousal network (Lovett-Barron et al., 2017). By modulating the wake-to-sleep sequence, the activity of EWcp neurons specifically prolongs the time window dedicated to nesting while also increasing the transitions toward nesting. Extending nesting phases before grooming serves a crucial purpose for the survival of the litter. As these neurons are present in all vertebrates, this suggests that preparatory nesting during pregnancy in some species such as the mouse is enabled indirectly by repurposing a neural mechanism controlling the extension of arousal during a wake-to-sleep sequence. This may indicate that parental behaviors could have appeared repeatedly throughout evolution by the exaptation (Gould and Vrba, 1982) (pre-adaptation) of homeostatic behaviors modulated by brain nuclei that control physiological states.

## STAR★METHODS

Detailed methods are provided in the online version of this paper and include the following:

- KEY RESOURCES TABLE
- RESOURCE AVAILABILITY
  - Lead contact
  - Material availability
  - Data and code availability
- EXPERIMENTAL MODEL AND SUBJECT DETAILS
  - Animals
- METHOD DETAILS
  - Stereotactic AAV injection
  - AAV ressources
  - Optical fiber implantation
  - Progesterone implantation and titration
  - Remote thermometry
  - Intracardiac PFA Perfusions
  - Immunohistochemistry
  - Antibodies
  - Fluorescent In-situ hybridization
  - iDISCO+ whole brain immunolabeling
  - Light sheet microscopy
  - Computing Resources
  - Manual daily nest scoring
  - Fos Mapping
  - Automated nesting segmentation
  - Parental nesting
  - Chemogenetics
  - Optogenetics
  - Fiber photometry
- QUANTIFICATION AND STATISTICAL ANALYSIS

### SUPPLEMENTAL INFORMATION

Supplemental information can be found online at https://doi.org/10.1016/j.neuron.2022.01.012.

(F) Sections at the level of the EW in mice injected with CNO or saline, immunolabeled for Fos and mCherry, showing the induction of Fos expression following CNO injection.

(G) Whole-brain mapping with iDISCO+ of Fos expression evoked by CNO injections in E15 pregnant females over saline-injected pregnant females, showing induction of Fos in the EW.

(H) Combined whole brain datasets of projection and activation patterns.

(I) Overlap of projection and activation maps reveals regions downstream of the EWcp$^{CART+}$ neurons in the preoptic areas and brainstem reticular formation.

(J) Volcano plot of Fos expression in brain regions induced by CNO over saline in CART-cre mice injected with AAV2-DIO-HM3Dq. Regions highlighted in green are also significantly activated during nesting (based on voxel maps) and receive projections from EWcp$^{CART+}$ neurons. Scale bars are 1 mm, except (F): 50 μm. Student's t test for (F), (I), and (J). See also Video S4.

**Neuron**
Article

**REFERENCES**

Bashour, N.M., and Wray, S. (2012). Progesterone directly and rapidly inhibits GnRH neuronal activity via progesterone receptor membrane Component 1. Endocrinology 153, 4457–4469.

Bridges, R.S. (2016). Long-term alterations in neural and endocrine processes induced by motherhood in mammals. Horm. Behav. 77, 193–203.

Brunton, P.J., and Russell, J.A. (2008). The expectant brain: adapting for motherhood. Nat. Rev. Neurosci. 9, 11–25.

Chaumont, F. de, Ey, E., Torquet, N., Lagache, T., Dallongeville, S., Imbert, A., Legou, T., Le Sourd, A.M., Faure, P., Bourgeron, T., et al. (2019). Real-time analysis of the behaviour of groups of mice via a depth-sensing camera and machine learning. Nat. Biomed. Eng. 3, 930–942.

Chettih, S.N., and Harvey, C.D. (2019). Single-neuron perturbations reveal feature-specific competition in V1. Nature 567, 334–340.

Dana, H., Sun, Y., Mohar, B., Hulse, B.K., Kerlin, A.M., Hasseman, J.P., Tsegaye, G., Tsang, A., Wong, A., Patel, R., et al. (2019). High-performance calcium sensors for imaging activity in neuronal populations and microcompartments. Nat. Methods 16, 649–657.

Deacon, R.M.J. (2006). Assessing nest building in mice. Nat. Protoc. 1, 1117–1119.

Dos Santos Júnior, E.D., Da Silva, A.V., Da Silva, K.R., Haemmerle, C.A., Batagello, D.S., Da Silva, J.M., Lima, L.B., Da Silva, R.J., Diniz, G.B., Sita, L.V., et al. (2015). The centrally projecting Edinger-Westphal nucleus–I: Efferents in the rat brain. J. Chem. Neuroanat. 68, 22–38.

Eban-Rothschild, A., Giardino, W.J., and Lecea, L. de. (2017). To sleep or not to sleep: neuronal and ecological insights. Curr. Opin. Neurobiol. 44, 132–138.

Eban-Rothschild, A., Rothschild, G., Giardino, W.J., Jones, J.R., and Lecea, L. de. (2016). VTA dopaminergic neurons regulate ethologically relevant sleep–wake behaviors. Nat. Neurosci. 19, 1356–1366.

Friedmann, D., Pun, A., Adams, E.L., Lui, J.H., Kebschull, J.M., Grutzner, S.M., Castagnola, C., Tessier-Lavigne, M., and Luo, L. (2020). Mapping mesoscale axonal projections in the mouse brain using a 3D convolutional network. Proc. Natl. Acad. Sci. USA 117, 11068–11075.

Giardino, W.J., Cote, D.M., Li, J., and Ryabinin, A.E. (2012). Characterization of genetic differences within the centrally projecting Edinger-Westphal nucleus of C57BL/6J and DBA/2J mice by expression profiling. Front. Neuroanat. 6, 5.

Gould, S.J., and Vrba, E.S. (1982). Exaptation—a missing term in the science of form. Paleobiology 8, 4–15.

Jirkof, P. (2014). Burrowing and nest building behavior as indicators of well-being in mice. J. Neurosci. Methods 234, 139–146.

Jirkof, P., Fleischmann, T., Cesarovic, N., Rettich, A., Vogel, J., and Arras, M. (2013). Assessment of postsurgical distress and pain in laboratory mice by nest complexity scoring. Lab Anim. 47, 153–161.

Johnstone, L.E., and Higuchi, T. (2001). Food intake and leptin during pregnancy and lactation. Prog. Brain Res. 133, 215–227.

Kapur, J., and Joshi, S. (2021). Progesterone modulates neuronal excitability bidirectionally. Neurosci. Lett. 744, 135619.

Keller, M., Vandenberg, L.N., and Charlier, T.D. (2019). The parental brain and behavior: a target for endocrine disruption. Front. Neuroendocrinol. 54, 100765.

Kirst, C., Skriabine, S., Vieites-Prado, A., Topilko, T., Bertin, P., Gerschenfeld, G., Verny, F., Topilko, P., Michalski, N., Tessier-Lavigne, M., and Renier, N. (2020). Mapping the fine-scale organization and plasticity of the brain vasculature. Cell 180, 780–795.e25.

Klapoetke, N.C., Murata, Y., Kim, S.S., Pulver, S.R., Birdsey-Benson, A., Cho, Y.K., Morimoto, T.K., Chuong, A.S., Carpenter, E.J., Tian, Z., et al. (2014). Independent optical excitation of distinct neural populations. Nat. Methods 11, 338–346.

Kohl, J. (2020). Parenting — a paradigm for investigating the neural circuit basis of behavior. Curr. Opin. Neurobiol. 60, 84–91.

Kohl, J., Autry, A.E., and Dulac, C. (2017). The neurobiology of parenting: a neural circuit perspective. Bioessays 39, 1–11.

Kohl, J., and Dulac, C. (2018). Neural control of parental behaviors. Curr. Opin. Neurobiol. 49, 116–122.

Komiya, H., Miyoshi, C., Iwasaki, K., Hotta-Hirashima, N., Ikkyu, A., Kanno, S., Honda, T., Gosho, M., Hamada, H., Satoh, T., et al. (2018). Sleep/wake behaviors in mice During pregnancy and pregnancy-associated hypertensive mice. Sleep 41, zsx209.

Kozicz, T., Bittencourt, J.C., May, P.J., Reiner, A., Gamlin, P.D.R., Palkovits, M., Horn, A.K.E., Toledo, C.A.B., and Ryabinin, A.E. (2011). The Edinger-Westphal nucleus: a historical, structural, and functional perspective on a dichotomous terminology. J. Comp. Neurol. 519, 1413–1434.

Krashes, M.J., Koda, S., Ye, C., Rogan, S.C., Adams, A.C., Cusher, D.S., Maratos-Flier, E., Roth, B.L., and Lowell, B.B. (2011). Rapid, reversible activation of AgRP neurons drives feeding behavior in mice. J. Clin. Invest. 121, 1424–1428.

Laursen, M., and Rekling, J.C. (2006). The Edinger-Westphal nucleus of the juvenile rat contains transient- and repetitive-firing neurons. Neuroscience 141, 191–200.

Li, X., Chen, W., Pan, K., Li, H., Pang, P., Guo, Y., Shu, S., Cai, Y., Pei, L., Liu, D., et al. (2018). Serotonin receptor 2c-expressing cells in the ventral CA1 control attention via innervation of the Edinger-Westphal nucleus. Nat. Neurosci. 21, 1239–1250.

Lim, M.M., Tsivkovskaia, N.O., Bai, Y., Young, L.J., and Ryabinin, A.E. (2006). Distribution of corticotropin-releasing factor and urocortin 1 in the vole brain. Brain Behav. Evol. 68, 229–240.

Lisk, R.D., Pretlow, R.A., and Friedman, S.M. (1969). Hormonal stimulation necessary for elicitation of maternal nest-building in the mouse (Mus musculus). Anim. Behav. 17, 730–737.

Lovett-Barron, M., Andalman, A.S., Allen, W.E., Vesuna, S., Kauvar, I., Burns, V.M., and Deisseroth, K. (2017). Ancestral circuits for the coordinated modulation of brain state. Cell 171, 1411–1423.e17.

Maynard, K.R., Hobbs, J.W., Phan, B.N., Gupta, A., Rajpurohit, S., Williams, C., Rajpurohit, A., Shin, J.H., Jaffe, A.E., and Martinowich, K. (2018). BDNF-TrkB signaling in oxytocin neurons contributes to maternal behavior. eLife 7, e33676.

Neumann, I.D., Johnstone, H.A., Hatzinger, M., Liebsch, G., Shipston, M., Russell, J.A., Landgraf, R., and Douglas, A.J. (1998). Attenuated neuroendocrine responses to emotional and physical stressors in pregnant rats involve adenohypophysial changes. J. Physiol. 508, 289–300.

**CellPress**
OPEN ACCESS

Parakala, M.L., Zhang, Y., Modgil, A., Chadchankar, J., Vien, T.N., Ackley, M.A., Doherty, J.J., Davies, P.A., and Moss, S.J. (2019). Metabotropic, but not allosteric, effects of neurosteroids on GABAergic inhibition depend on the phosphorylation of GABAA receptors. J. Biol. Chem. 294, 12220–12230.

Pomrenze, M.B., Walker, L.C., and Giardino, W.J. (2021). Gray areas: neuropeptide circuits linking the Edinger-Westphal and Dorsal Raphe nuclei in addiction. Neuropharmacology 198, 108769.

Priest, M.F., Freda, S.N., Badong, D., Dumrongprechachan, V., and Kozorovitskiy, Y. (2021). Peptidergic modulation of fear responses by the Edinger-Westphal nucleus. bioRxiv. https://doi.org/10.1101/2021.08.05.455317.

Ranson, S.W., and Magoun, H.W. (1933). The central path of the pupilloconstrictor reflex in response to light. Arch. Neurol. Psychiatry 30, 1193–1204.

Renier, N., Adams, E.L., Kirst, C., Wu, Z., Azevedo, R., Kohl, J., Autry, A.E., Kadiri, L., Umadevi Venkataraju, K.U., Zhou, Y., et al. (2016). Mapping of brain activity by automated volume analysis o f immediate early genes. Cell 165, 1789–1802.

Ryabinin, A.E., Cocking, D.L., and Kaur, S. (2013). Inhibition of VTA neurons activates the centrally projecting Edinger-Westphal nucleus: evidence of a stress-reward link? J. Chem. Neuroanat. 54, 57–61.

Sahores, A., Luque, G.M., Wargon, V., May, M., Molinolo, A., Becu-Villalobos, D., Lanari, C., and Lamb, C.A. (2013). Novel, low cost, highly effective, hand-made steroid pellets for experimental studies. PLoS One 8, e64049.

Schneider, C.A., Rasband, W.S., and Eliceiri, K.W. (2012). NIH Image to ImageJ: 25 years of image analysis. Nat. Methods 9, 671–675.

Shamonin, D.P., Bron, E.E., Lelieveldt, B.P., Smits, M., Klein, S., and Staring, M.; Alzheimer's Disease Neuroimaging Initiative (2013). Fast parallel image registration on CPU and GPU for diagnostic classification of Alzheimer's disease. Front. Neuroinform. 7, 50.

Silva, A.V. da, Torres, K.R., Haemmerle, C.A., Céspedes, I.C., and Bittencourt, J.C. (2013). The Edinger–Westphal nucleus II: hypothalamic afferents in the rat. J. Chem. Neuroanat. 54, 5–19.

Smarr, B.L., Zucker, I., and Kriegsfeld, L.J. (2016). Detection of successful and unsuccessful pregnancies in mice within hours of pairing through frequency analysis of high temporal resolution core body temperature data. PLoS one 11, e0160127.

Sotelo, Maria I., et al. (2022). Lateral hypothalamic neuronal ensembles regulate pre-sleep nest-building behavior. Current Biology 32, 1–17. https://doi.org/10.1016/j.cub.2021.12.053.

Vesuna, S., Kauvar, I.V., Richman, E., Gore, F., Oskotsky, T., Sava-Segal, C., Luo, L., Malenka, R.C., Henderson, J.M., Nuyujukian, P., et al. (2020). Deep posteromedial cortical rhythm in dissociation. Nature 586, 87–94.

Wang, Q., Ding, S.L., Li, Y., Royall, J., Feng, D., Lesnar, P., Graddis, N., Naeemi, M., Facer, B., Ho, A., et al. (2020). The Allen Mouse Brain Common coordinate framework: a 3D reference atlas. Cell 181, 936–953.e20.

Xu, L., Janssen, D., Knaap, N. van der, Roubos, E.W., Leshan, R.L., Myers, M.G., Gaszner, B., and Kozicz, T. (2014). Integration of stress and leptin signaling by CART producing neurons in the rodent midbrain centrally projecting Edinger-Westphal nucleus. Front. Neuroanat. 8, 8.

Xu, L., Scheenen, W.J.J.M., Leshan, R.L., Patterson, C.M., Elias, C.F., Bouwhuis, S., Roubos, E.W., Myers, M.G., and Kozicz, T. (2011). Leptin signaling modulates the activity of urocortin 1 neurons in the mouse nonpreganglionic Edinger-Westphal nucleus. Endocrinology 152, 979–988.

Xu, X., Coats, J.K., Yang, C.F., Wang, A., Ahmed, O.M., Alvarado, M., Izumi, T., and Shah, N.M. (2012). Modular genetic control of sexually dimorphic behaviors. Cell 148, 596–607.

Yang, C.F., Chiang, M.C., Gray, D.C., Prabhakaran, M., Alvarado, M., Juntti, S.A., Unger, E.K., Wells, J.A., and Shah, N.M. (2013). Sexually dimorphic neurons in the ventromedial hypothalamus govern mating in both sexes and aggression in males. Cell 153, 896–909.

Yushkevich, P.A., Piven, J., Hazlett, H.C., Smith, R.G., Ho, S., Gee, J.C., and Gerig, G. (2006). User-guided 3D active contour segmentation of anatomical structures: significantly improved efficiency and reliability. NeuroImage 31, 1116–1128.

Zhang, Z., Zhong, P., Hu, F., Barger, Z., Ren, Y., Ding, X., Li, S., Weber, F., Chung, S., Palmiter, R.D., and Dan, Y. (2019). An excitatory circuit in the perioculomotor midbrain for non-REM sleep control. Cell 177, 1293–1307.e16.

Zuniga, A., and Ryabinin, A.E. (2020). Involvement of centrally projecting Edinger–Westphal nucleus neuropeptides in actions of addictive drugs. Brain Sci. 10, 67.

**CellPress**
OPEN ACCESS

**Neuron**
Article

## STAR★METHODS

### KEY RESOURCES TABLE

| REAGENT or RESOURCE | SOURCE | IDENTIFIER |
|---|---|---|
| **Antibodies** | | |
| Rabbit polyclonal anti-Ucn1 | Sigma-Aldrich | Cat#U4757; RRID: AB_261834 |
| Goat polyclonal anti-CART | R&D System | Cat#AF163; RRID: AB_2068569 |
| Chicken polyclonal anti-GFP | Aves Labs | Cat#GFP-1020; RRID: AB_10000240 |
| Goat polyclonal anti-RFP | Rockland | Cat#200-101-379; RRID: AB_2744552 |
| Rabbit polyclonal anti-mPR$\beta$ (PAQR8) | Bioss | Cat#BS11410R; RRID: N/A |
| Rabbit polyclonal anti-mPR$\gamma$ (PAQR5) | Abcam | Cat#ab236798; RRID: N/A |
| Rabbit polyclonal anti-Fos | Synaptic Systems | Cat#226-003; RRID: AB_2231974 |
| Guinea-Pig polyclonal anti-Fos | Synaptic Systems | Cat#226-004; RRID: AB_2619946 |
| Mouse monoclonal anti-NeuN | Millipore | Cat#MAB377; RRID: AB_2298772 |
| Rabbit polyclonal anti-PGR | Sigma-Aldrich | Cat#SAB4502184; RRID: AB_10746273 |
| **Bacterial and virus strains** | | |
| pAAV-flex-taCasp3-TEVp | Yang et al., 2013 | Addgene_45580 |
| AAV9-EF1a-DIO-ChrimsonR-mRuby2-KV2.1-WPRE-SV40 | Chettih and Harvey, 2019 | Addgene AAV9; 124603-AAV9 |
| AAV2-Ef1a-DIO-EYFP | Karl Deisseroth Lab | Addgene AAV2; 27056-AAV2 |
| AAV1-syn-FLEX-jGCaMP7s-WPRE | Dana et al., 2019 | Addgene AAV1; 104491-AAV1 |
| AAV2-hSyn-DIO-hM3D(Gq)-mCherry | Krashes et al., 2011 | Addgene AAV2; 44361-AAV2 |
| AAV2-hSyn-DIO-mCherry | Bryan Roth Lab | Addgene AAV2; 50459-AAV2 |
| AAV2-hSyn-DIO-hM4D(Gi)-mCherry | Krashes et al., 2011 | Addgene AAV2; 44362-AAV2 |
| AAV1-CMV-SaCAS9-U6-gRNA(Ucn) | GeneCopoeia | Cat#AA01- MCP001598-AD01-3-200(a,b,c) |
| AAV1-CMV-SaCAS9-U6-gRNA(CART) | GeneCopoeia | Cat#217AA01-MCP299483-AD01-3-200 |
| AAV1-CMV-SaCAS9-U6-gRNA(Cck) | GeneCopoeia | Cat#217AA01-MCP291368-645 AD01-3-200(a,b,c) |
| AAV1-CMV-SaCAS9-U6-gRNA(Scrambled) | GeneCopoeia | Cat#217AA01-CCPCTR01-AD01-100 |
| **Chemicals, peptides, and recombinant proteins** | | |
| Progesterone | Sigma-Aldrich | Cat#5341; CAS: 57-83-0 |
| Clozapine N-oxide | Enzo life sciences | Cat#BML-NS105-0025; CAS: 34233-69-7 |
| **Critical commercial assays** | | |
| RNAscope Multiplex Fluorescent Reagent Kit v2 | ACDbio | Cat#320293 |
| Mouse Progesterone ELISA Kit | Novus Biological | Cat#NBP2-60125-1 |
| **Experimental models: Organisms/strains** | | |
| Mouse: C57BL6/NRj | Janvier Labs | Cat# 028533 |
| Mouse: B6;129S- Cartpt$^{tm1.1(cre)Hze}$/J | The Jackson Laboratory | JAX: 028533 |
| Mouse: B6.Cg-$Gt(ROSA)26Sor^{tm14(CAG-tdTomato)Hze}$/J | The Jackson Laboratory | JAX: 007914 |

# Neuron
## Article

CellPress
OPEN ACCESS

*Continued*

| REAGENT or RESOURCE | SOURCE | IDENTIFIER |
|---|---|---|
| Software and algorithms | | |
| ImageJ | Schneider et al., 2012 | https://imagej.nih.gov/ij/ |
| Imaris | Oxford Instruments | https://imaris.oxinst.com |
| ITK-SNAP | Yushkevich P.A. et al., 2006 | http://www.itksnap.org |
| ClearMap2 | Kirst C. et al., 2021 and this paper | https://github.com/ChristophKirst/ClearMap2 https://doi.org/10.5281/zenodo.3924619 |
| TrailMap | Friedmann D. et al., 2020 | https://github.com/AlbertPun/TRAILMAP |
| TopMouseTracker | This paper | https://github.com/Tom-top/TopMouseTracker https://doi.org/10.5281/zenodo.5833515 |

## RESOURCE AVAILABILITY

### Lead contact
Further information and requests for resources and reagents may be directed to and will be fulfilled by the lead contact, Dr. Nicolas Renier (nicolas.renier@icm-institute.org).

### Material availability
This paper doesn't report original biological material.

### Data and code availability
The latest version of the code for ClearMap 2.0 is available at https://github.com/ChristophKirst/ClearMap2. https://doi.org/10.5281/zenodo.3924619

The latest version of the code for automated nesting segmentation is available at https://github.com/Tom-top/TopMouseTracker. A pre-release version is available at https://doi.org/10.5281/zenodo.5833515

Any information required to obtain and reanalyze the data reported in this paper is available from the lead contact upon request.

## EXPERIMENTAL MODEL AND SUBJECT DETAILS

### Animals
All procedures followed the European legislation for animal experimentation (directive 2010/63/EU). Animal manipulations were approved by the institutional Ethical Committee (Project 8461-2017010619499922). Male and female C57BL6/NRj mice and vasec-tomized C57BL6/NRj male mice obtained from Janvier Labs (France). CART-cre mice, or B6;129S-Cartpttm1.1(cre)Hze/J, were obtained from Jackson Laboratories (stock 028533), kept as hemizygotes, and back-crossed to C57BL6/NRj in every generation. Rosa26-lsl-tdTomato reporter line (Ai14), or B6;129S6-Gt(ROSA)26Sortm14(CAG-tdTomato)Hze/J, was obtained from Jackson Laboratories (stock 007914).

Upon arrival, the mice were kept in an acclimatization sector for a one-week period to get habituated to our facilities before housing in the general sector. Mice were bred and maintained at the specific pathogen free mouse facility of Paris Brain Institute, with controlled temperature (21 ± 1°C) and humidity (40-70%), ad libitum access to standard mouse chow and water, and on a 12h:12h light/dark cycle (lights on at 8AM). Lighting cycles with a controlled rising and decreasing gradient at 8am / 8pm respectively, simulating natural light. Mice were housed in groups of 3-6 during experiments or single housed when nesting abilities were evaluated.

## METHOD DETAILS

### Stereotactic AAV injection
Mice were anesthetized under isoflurane (4% for induction; 1,8% for maintenance; oxygen at 250 ml/min). S.c. buprenorphine (0.1 mg/kg) was administered to prevent pain. Local lidocaine 0.5% (0.1ml) was also administered after shaving the head. Mice were positioned in a stereotaxic frame (Kopf Instruments, California) to target the EWcp using Lambda coordinates according to Pax-inos & Franklin Mouse Brain Atlas: A/P, +0.40 mm (-3.80 mm from Bregma); M/L, 0.94 mm; D/V, -3.62 mm; 15° angle. Ophthalmic ointment was applied to the eyes. A midline incision was made down the scalp and a craniotomy was made using a micro drill (0.5mm tip diameter: FST # 19007-05). A 10 μl Hamilton syringe (1701RN; Phymep, France) with a 34-gauge metal needle was used to infuse 500 nl virus at a rate of 50 nl/min to ensure that the full rostro-caudal extent of the EW nucleus was infected. The needle was kept at

the injection site for 15 min once the infusion has finished and then, slowly withdrawn. Skin was sutured using Vicryl 6.0R and mice stayed in a chamber at 37°C the time required to fully recover. To prevent any pain due to surgery, analgesic treatment was followed for 48 h with s.c. Carprofen (5 mg/kg each 24h).

### AAV ressources

The following Adeno-Associated Viruses were used: CRISPR AAVs expressing saCas9 and gRNA against Ucn1, CCK and CART were obtained from GeneCopoeia (MA, USA). 3 AAVs expressing different gRNAs were obtained for each gene. Catalogue numbers are AA01-MCP001598-AD01-3-200 a, b and c (UCN1, both variants GenBank:NM_021290.2 & GenBank:NM_001346010.1), 217AA01-CCPCTR01-AD01-100 (scrambled), 217AA01-MCP291368-AD01-3-200 a, b and c (CCK, GenBank:NM_031161.4) and 217AA01-MCP299483-AD01-3-200 (Cartpt, GenBank:NM_013732.7). AAV1-flex-taCasp3-TEVp (Yang et al., 2013) DNA was obtained from Addgene (ref. 45580) and produced at the Paris Brain Institute viral core facility. pAAV-EF1a-DIO-ChrimsonR-mRuby2-KV2.1-WPRE-SV40 (Chettih and Harvey, 2019) AAV9 particules were obtained from Addgene (ref 124603-AAV9). pAAV-Ef1a-DIO-EYFP AAV2 particules were obtained from Addgene (ref 27056-AAV2). pGP-AAV-syn-FLEX-jGCaMP7s-WPRE (AAV1) (Dana et al., 2019) AAV1 particules were obtained from Addgene (ref 104491-AAV1). pAAV-hSyn-DIO-hM3D(Gq)-mCherry, pAAV-hSyn-DIO-mCherry and pAAV-hSyn-DIO-hM4D(Gi)-mCherry AAV2 particules (Krashes et al., 2011) were obtained from Addgene (ref 44361-AAV2, 50459-AAV2 and 44362-AAV2).

### Optical fiber implantation

Mice were anesthetized and virus infusion in the EWcp was done as above, but with no angle (Lambda coordinates according to Paxinos & Franklin: A/P, +0.60 mm mm (-3.60 mm from Bregma); M/L, 0.0 mm; D/V, -3.6 mm). After withdrawing the needle, an optic fiber cannula (1.25 mm OD, 400 μm, 0.50 NA, 5 mm length) was implanted at the midline into the EWcp (same coordinates except from D/V, -3.2 mm) and was cemented to the skull by dental resin cement (Super-Bond, C&B). Mice stayed in a chamber at 37°C the time required to fully recover. To prevent any pain due to surgery, analgesic treatment was followed for 48 h with s.c. Carprofen (5 mg/kg each 24h).

### Progesterone implantation and titration

Progesterone pellets were prepared in house according to Sahores et al. (Sahores et al., 2013). Progesterone (Sigma) was thoroughly mixed with the dimethyl siloxane-containing multi-purpose sealant (Dowsil 732™) using plastic tips, during 10 minutes. We mixed 100 mg progesterone + 300 mg Dowsil. The mixture was pressed between glass slides wrapped in greaseproof paper and left to harden overnight. The following day, the tablet was weighed and cut in pieces of 20 mg, 60 mg, or 100 mg for obtaining progesterone pellets of 5mg, 15 mg, or 25 mg, respectively.

Progesterone implantation: Mice were anesthetized under isoflurane (4% for induction; 1,8% for maintenance; oxygen at 250 ml/min). S.c. buprenorphine (0.1 mg/kg) was administered to prevent pain. Mice were positioned over a heat pad at 37°C and a 3-4 mm incision was made through the skin, dorsally on the neck. A small pellet of progesterone was placed in the subcutaneous tissue and the skin was sutured using Vicryl 6.0. Mice stayed in a chamber at 37°C the time required to fully recover. To prevent any pain due to surgery, analgesic treatment was followed for 24 h with s.c. Carprofen (5 mg/kg).

For circulating Progesterone titration, a drop of blood was sampled from the mouse cheek, and processed through a Mouse Progesterone ELISA kit according to the manufacturer's instructions (Novus Biological NBP2-60125-1).

### Remote thermometry

Mice were anesthetized under isoflurane (4% for induction; 1,8% for maintenance; oxygen at 250 ml/min). S.c. buprenorphine (0.1 mg/kg) was administered to prevent pain. Mice were positioned over a heat pad at 37°C. Following shaving and topic antiseptic application, access to the peritoneal cavity was gained through a 8-9 mm incision in the midline. A miniaturized electronic capsule (Anipill®; 1.7g) was placed into the abdominal cavity. Incision was closed with resorbable (Vicryl 6.0R) inner suture and nonresorbable (Nylon 6.0) outer suture. Mice stayed in a chamber at 37°C the time required to fully recover. To prevent any pain due to surgery, analgesic treatment was followed for 48 h with s.c. Carprofen (5 mg/kg). Continuous monitoring of Tc at 5-min intervals was performed for the duration of the experiments.

### *In vitro slice electrophysiology: Slice preparation*

Acute coronal brain slices (300μm) were obtained from 2 months-old virgin and E12-E15 pregnant female Cart-Cre mice injected with a Cre-dependent eYFP AAV expressing eYFP in the EW for evoked firing. Virus injection was performed at least one week before the recordings. Animals were deeply anesthetized with pentobarbital (200mg/100g of animal, Euthasol Vet) and perfused through the heart with an ice-cold (4°C) sucrose-based cutting solution containing (in mM): 200 sucrose, 26 NaHCO3, 2.5 KCl, 1.25 NaH2PO4, 7 MgSO4, 0.5 CaCl2, 3 pyruvic acid, 3 myo-inositol, 0.4 ascorbic acid and 16 glucose, saturated with 95% O2 / 5% CO2. Brains were quickly removed and immersed in the same cutting solution. Slices were cut with a vibratome (Leica) in cutting solution and incubated in oxygenated artificial cerebrospinal fluid (aSCF) containing (in mM): 126 NaCl, 2.5 KCl, 2 CaCl2, 1 MgSO4, 1.25 NaH2PO4, 26 NaHCO$_3$ and 16 glucose, equilibrated with 95% O2 / 5% CO2 (pH 7.4), initially at 34°C for 30 min, and subsequently at room temperature, before being transferred to the recording chamber. Whole cell patch-clamp recordings were obtained at 30°C from visually identified GFP+ CART neurons of the EW. Glass electrodes (tip resistance of 2-4 MΩ) were filled with the following solution (in mM):

# Neuron
## Article

**CellPress**
OPEN ACCESS

133 K-gluconate, 11 KCl, 10 HEPES, 0.2 EGTA, 4 Mg-ATP, 0.3 Na-GTP, 4 Na-phosphocreatine; pH adjusted to 7.2 with KOH; 280-300 mOsm. The estimated $E_{Cl}$ was approximately -65 mV based on the Nernst equation, without correction for gluconate-generated liquid junction potential. Spontaneous AMPA receptor-mediated excitatory synaptic events were pharmacologically isolated in the presence of 50 μm picrotoxin (0.0005% DMSO final) and 50 μm D-(-)-2-Amino-5-phosphonopentanoic acid (D-AP5) in the aCSF bath perfusion to block inhibitory GABAA receptors-mediated and glutamatergic NMDA receptor-mediated synaptic events, respectively, and recorded in voltage-clamp mode at a holding potential of -70 mV. During current clamp recordings, slices were continuously perfused with aCSF containing 20 μm 6,7-Dinitroquinoxaline-2,3-dione (DNQX), an AMPA/kainate receptor antagonist in addition to picrotoxin and D-AP5 to completely block fast inhibitory and excitatory synaptic transmission. For progesterone incubations, 1 μM progesterone (Sigma) was added to the superfused bath aCSF supplemented with glutamatergic and GABAergic synaptic blockers (DNQX, D-AP5 and picrotoxin). Since progesterone was dissolved initially in DMSO, the vehicle was added also to the control solution at the same concentration (DMSO 0.0005%). For all experiments, DMSO never exceeded 0.001% and was systematically present at the same concentration when different solutions were tested on the same cell. 5 cells in 5 mice were recorded with DMSO, and 9 cells in 6 mice with progesterone. All drugs were obtained from Hello Bio (Bristol, UK) or Merck (Sigma).

### In vitro slice electrophysiology: Data acquisition and analysis

Signals were amplified with a Multiclamp 700B amplifier (Molecular devices), sampled at 20 kHz and filtered at 2 kHz in voltage clamp mode, sampled at 20 or 50 kHz for spontaneous or evoked membrane voltage, respectively, and filtered at 10 kHz in current clamp mode. Data were analyzed using pClamp (Molecular Devices), Prism (GraphPad) software and custom written scripts (MATLAB, Math works). Glutamatergic synaptic currents were detected with custom written software (Wdetecta, courtesy of J. R. Huguenard, Stanford University).

In voltage-clamp experiments, access resistance was on average <20 MΩ and carefully monitored with small voltage steps (-5 mV for 50 ms; repeated 50 times). Data were discarded from analysis if resistance changes exceeded 20% during the recorded period. Spontaneously occurring excitatory postsynaptic current (sEPSC) were recorded at a holding potential of -70 mV (13 cells in 6 mice (virgins) and 18 cells in 6 mice (pregnant). For each cell, the amplitude of individual sEPSC were measured over a 1 to 3 min time window (with at least 200 events per cell) and the mean amplitude and frequency calculated over this period.

In current-clamp experiments, input resistance was monitored with small current steps (−10 pA for 500 ms; repeated 30 times) and cells were excluded if it changed by > 25%.

The evoked firing properties were determined in response to a series of consecutive 1 s long current steps increasing by 20 pA from -100 pA up to depolarizing values reaching spiking saturation (when possible), while maintaining the baseline membrane potential at -70 mV. Action potentials (AP) were detected using a threshold criterion and the mean firing frequency was calculated (number of action potentials/s) for each step. The time of each AP peak was used to calculate interspike interval (ISI) times defined as:

$$\Delta ti = t_i - t_{i-1}$$

and the ISI coefficient of variation as following:

$$CV = \frac{\sigma}{\mu}$$

σ is the population standard deviation; μ is the population mean.

The mean firing frequency was plotted as input-ouput relationships (IO curve) for individual cell and used to determine their evoked firing pattern. Cells with a repetitive spiking pattern were characterized by a mean firing frequency IO relationship with a sigmoidal shape and a maximal frequency (> 15 Hz), in combination with a ISI CV small and stable resulting in an IO curve with a linear profile and a slightly positive slope over increasing depolarizing steps. By contrast, cells with a transient firing generated only very few AP distributed almost exclusively as a burst at the onset of the current steps, resulting in a very low mean firing frequency (<6 Hz) and a stair profile of the corresponding IO, together with a ISI CV inexistent (for the steps with less than 2 evoked AP) or highly variable (when a spike occasionally occurs later during a step). Finally, a third intermediate subpopulation of cells fired spikes both as burst at the onset of the current step and irregularly later during the steps resulting in a IO relationship profile for the mean frequency either scattered or sigmoidal-like but with a maximum < 15 Hz, in combination with an irregular ISI CV. For evoked firing, 11 cells were recorded in 5 virgin mice and 16 cells in 6 pregnant mice.

Since almost all Cart+ neurons were spontaneously spiking at resting potential, we also detected spontaneous spikes using a threshold criterion and calculated the mean firing frequency over 5 min bin time window. The effect of progesterone was tested on both spontaneous spiking and evoked firing pattern.

Input resistance (Ri) was calculated from the average steady state potential during the final 50 ms of the voltage deflection in response to 500 ms long current steps of -10 pA repeated 30 times, relative to the preceding 50 ms baseline. The membrane time constant (τm) was determined by fitting a single exponential function to the curve of the average membrane potential obtained in response to the negative current step. The membrane capacitance (Cm) was calculated as follows:

$$\tau_m = R_i \times C_m$$

From the current clamp voltage responses to a series of 1 s long current steps, used to evaluate the spiking firing properties, we measured also the rheobase, defined as the minimal current triggering an AP. However, the 20 pA increment limited the accuracy of

**CellPress**
OPEN ACCESS

**Neuron**
Article

this estimation. Moreover, the hyperpolarization-activated cation current (Ih) was estimated from the sag in the membrane potential in response to negative current steps from -100 to -40 pA. The sag is defined by the difference between the peak potential and the steady state potential during the final 100 ms of the current step. Sag potential were normalized to the respective peak voltage deflection from the baseline membrane potential (before the step) and the average of the normalized sag potential used as an estimate of Ih for each neuron.

For calcium imaging during the evoked firing protocol, images were acquired with a Nikon DS-Qi2 camera at 10 fps. The analysis of calcium signals was performed with a custom python script: a region of interest (ROI), enclosing the soma of the recorded cell, was determined, and the mean pixel value was computed, over time, within the ROI. To account for photobleaching, the signal was corrected: the baseline signal was determined using the asymmetric least squares smoothing algorithm and subtracted from the original signal. The corrected signal was then standardized and compared between the different firing behaviors.

### Intracardiac PFA Perfusions

All animals were sacrificed by Pentobarbital overdose (200mg/100g of animal). Intracardiac perfusion was then performed with a peristaltic pump (Gilson, USA). Blood was washed by infusing 10mL of cold PBS followed by tissue fixation with 60mL of cold 4% Paraformaldehyde (Electron Microscopy Sciences, USA) diluted in PBS. Then brain dissection was quickly done taking special care to preserve the brain structure. Finally, the brains were then postfixed for 2 hours at room temperature by immersion in 4% Paraformaldehyde, and stored in PBS at 4°C until further processing.

### Immunohistochemistry

Perfused brains were equilibrated in 30% sucrose/PBS solution for 48h at 4°c and cut at 35μm on a freezing sliding microtome at -20°c. Floating sections were blocked in PBS-Tween 0.2% with 7.5% of Gelatin (Sigma) for 1h, and then incubated overnight at room temperature (about 23°c) with the primary antibodies diluted in the blocking solution. Sections were washed in PBS-Tween 0.2% 3 times for 30 minutes, and then incubated for 2h with the secondary antibody diluted in the blocking solution, supplemented with bis-benzimide (Sigma). Finally, the sections were washed and mounted in Mowiol. Images were acquired with a spinning disk microscope (3i), or with an epifluorescence Apotome (Zeiss). Images were analyzed with ImageJ (Schneider et al., 2012).

### Antibodies

The following primary antibodies were used: rabbit anti-Ucn1 at 1/2000th (Sigma U4757), goat anti-CART at 1/2000th (R&D systems AF163), chicken anti-GFP at 1/3000th (Aves GFP-1020), Goat anti-RFP at 1/1000th (Rockland 200-101-379), rabbit anti-PAQR8/mPRβ at 1/1000th (Bioss USA, BS11410R), rabbit anti-PAQR5/mPRγ at 1/1000th (Abcam ab236798), rabbit anti-Fos at 1/3000th (Synaptic Systems 226-003), guinea pig anti-Fos at 1/1000th (Synaptic Systems 226-004), mouse anti-NeuN at 1/1000th (Millipore MAB377), rabbit anti-Progesterone Receptor at 1/500th (Sigma SAB4502184).

Secondary antibodies raised in donkeys and coupled with either Alexa488, Alexa555 or Alexa647 were sources from Thermo Fisher Scientific and used at 1/1000th.

### Fluorescent In-situ hybridization

Perfused and dissected brains were incubated in a solution of 30% sucrose in PBS (w/v) for 48h and frozen in -40°C isopentane. Using a cryostat, 10μm-thick sections were cut and collected on Superfrost+ slides.

After air-drying the slides at room temperature, RNAscope® Hydrogen Peroxyde solution were added for 10 minutes. Slides were then incubated 10 minutes at 95°C in the RNAscope® Target Retrieval Reagents and then transferred in 100% alcohol for 3 minutes. Slides were treated with RNAscope® Protease III for 15min at 40°C. RNA oligomeric probes hybridization were performed for 2h at 40°C. RNA amplification was performed according to the protocol of the RNAscope Multiplex Fluorescent Reagent Kit v2 (Cat. No. 320293) using the fluorophores Opal 540 and 650 for dual FISH. For some experiments, the FISH was then followed by immunohistochemistry against CART or Ucn1.

ACDbio RNAscope probes used: Mm-CCK-C2 (402271-C2), Mm-Cartpt-C2 (432001-C2), Mm-Ucn (466261), Mm-Slc17a6 (319171), Mm-Slc17a7 (416631), Mm-Slc-17a8 (431261), Mm-Slc32a1 (319191).

### iDISCO+ whole brain immunolabeling

Whole brain staining was performed following the iDISCO+ protocol previously described previously (Renier et al., 2016) with minimal modifications. All the steps of the protocol were done at room temperature with gentle shaking unless otherwise specified. All the buffers were supplemented with 0,01% Sodium Azide (Sigma-Aldrich, Germany) to prevent bacterial and fungal growth.

Perfused brains were dehydrated in an increasing series of methanol (Sigma-Aldrich, France) dilutions in water (washes of 1 hour in methanol 20%, 40%, 60%, 80% and 100%). An additional wash of 2 hours in methanol 100% was done to remove residual water. Once dehydrated, samples were incubated overnight in a solution containing a 66% dichloromethane (Sigma-Aldrich, Germany) in methanol, and then washed twice in methanol 100% (4 hours each wash). Samples were then bleached overnight at 4°C in methanol containing a 5% of hydrogen peroxide (Sigma-Aldrich). Rehydration was done by incubating the samples in methanol 60%, 40% and 20% (1 hour each wash). After methanol pretreatment, samples were washed in PBS twice 15 minutes and 1 hour in PBS containing a 0,2% of Triton X-100 (Sigma-Aldrich) and further permeabilized by a 24 hours incubation at 37°C in *Permeabilization Solution*,

**Neuron**
**Article**

**CellPress**
OPEN ACCESS

composed by 20% dimethyl sulfoxide (Sigma-Aldrich), 2,3% Glycine (Sigma-Aldrich, USA) in PBS-T. In order to start the immunostaining, samples were first blocked with 0,2% gelatin (Sigma-Aldrich) in PBS-T for 24 hours at 37°C, the same blocking buffer was used to prepare antibody solutions. Primary antibodies were incubated for 10 days at 37°C with gentle shaking, then washed in PBS-T (twice 1 hour and then overnight), and finally newly incubated for 10 days with secondary antibodies. Secondary antibodies raised in donkeys, conjugated to Alexa 647 were used (Life Technologies). After immunostaining, the samples were washed in PBS-T (twice 1 hour and then overnight), dehydrated in a methanol/water increasing concentration series (20%, 40%, 60%, 80%, 100% one hour each and then methanol 100% overnight), followed by a wash in 66% dichloromethane – 33% methanol for 3 hours. Methanol was washed out with two final washes in dichloromethane 100% (15 min each) and finally the samples were cleared and stored in dibenzyl ether (Sigma-Aldrich) until light sheet imaging.

### Light sheet microscopy

The acquisitions were done on a LaVision Ultramicroscope II equipped with infinity-corrected objectives. The microscope was installed on an active vibration filtration device, itself put on a marble compressed-air table. Imaging was done with the following filters: 595/40 for Alexa Fluor-555, and -680/30 for Alexa Fluor-647. The microscope was equipped with the following laser lines: OBIS-561nm 100mW, OBIS-639nm 70mW, and used the 2nd generation LaVision beam combiner. The images were acquired with an Andor CMOS sNEO camera. Main acquisitions were done with the LVMI-Fluor 4X/O.3 WD6 LaVision Biotec objective. The microscope was connected to a computer equipped with SSD drives to speed up the acquisition.

The brain was positioned in sagittal orientation, cortex side facing the light sheet, to maximize image quality and consistency.

A field of view of 1000 x 1300 pixels was cropped at the center of the camera sensor. The light sheet numerical aperture was set to NA-0.03. The 3 light sheets facing the cortex were used, while the other side illumination was deactivated to improve the axial resolution. Beam width was set to the maximum. Laser powers were set to 40-60% (639nm). The center of the light sheet in x was carefully calibrated to the center of the field. z steps were set to 6μm. Tile overlaps were set to 10%. The whole acquisition takes about 1h per hemisphere.

At the end of the acquisition, the objective is changed to a MI PLAN 1.1X/0.1 for the reference scan at 488nm excitation (tissue autofluorescence). The field of view is cropped to the size of the brain, and the z-steps are set to 6μm, and light sheet numerical aperture to 0.03 NA. It is important to crop the field of view to the size of the brain for subsequent alignment steps.

### Computing Resources

The data were automatically transferred every day from the acquisition computer to a Lustre server for storage. The processing with ClearMap was done on local workstations, either Dell Precision T7920 or HP Z840. Each workstation was equipped with 2 Intel Xeon Gold 6128 3.4G 6C/12T CPUs, 512Gb of 2666MHz DDR4 RAM, 4x1Tb NVMe Class 40 Solid State Drives in a RAID0 array (plus a separate system disk), and an NVIDIA Quadro P6000, 24Gb VRAM video card. The workstations were operated by Linux Ubuntu 20.04LTS. ClearMap 2.0 was used on Anaconda Python 3.7 environment.

### Data analysis: ClearMap Fos+ cell counting

Tiled acquisitions of Fos-immunolabeled iDISCO+ cleared brains scanned with the light sheet microscope were processed with ClearMap 2 (https://github.com/ChristophKirst/)(Kirst et al., 2020; Renier et al., 2016) to generate both voxel maps of Fos cell densities, as well as region-based statistics of cell counts. The stitching was done with Wobbly Stitcher (Kirst et al., 2020) and the cell detection was run with parameters and filters identical to our previous work (Renier et al., 2016). Stitched images were processed for background removal, on which local maxima were detected to place initial seeds for the cells. A watershed was done on each seed to estimate the volume of the cell, and the cells were filtered according to their volume to exclude smaller artefactual maxima.

The alignment of the brain to the Allen Brain Atlas (March 2017) was based on the acquired autofluorescence image using Elastix (https://elastix.lumc.nl)(Shamonin et al., 2013). Filtered cell's coordinates were transformed to their reference coordinate in the Allen Brain Atlas common coordinate system (Wang et al., 2020). For voxel maps, spheres of 375μm diameter were drawn on each filtered cell. P-Value maps of significant differences between groups were generated using Mann-Whitney U test (SciPy implementation). Aligned voxelized datasets from each group of animals were manually inspected to identify the regional overlaps of p-value clusters, and volcano-plots of regional counts where generated.

ITK-Snap (Yushkevich et al., 2006) was used to manually annotate the EWcp nucleus, based on a scan of iDISCO+-labeled brain with CART aligned onto the 25μm template.

### Data analysis: TrailMap and TubeMap axon segmentation

Data for axon mapping were acquired the same way as for Fos mapping, and stitched with Wobbly Stitcher (Kirst et al., 2020). Stitched raw images were segmented with TrailMap (Friedmann et al., 2020) and a binary mask generated using a probability threshold of 0.5. The binary mask was then processed through Tube Map(Kirst et al., 2020) to obtain a skeleton of the axon traces, and then a graph representation aligned to the reference atlas. Quantifications of axon densities were obtained from the coordinates of both branching and non-branching points of the graph.

### Manual daily nest scoring

Females were isolated in separate cages prior to the start of the experiment for 4 to 6 days. Every morning at 10am, nests were manually scored, blind to the condition, using a modified version of the 5-points Deacon's scale (Deacon, 2006), from 0 to 4. 0 : Nesting

material is not shredded, no visible nest site; 1 : Nesting material is completely or partially shredded, identifiable nest but flat; 2 : Nesting material is completely or partially shredded, saucer shaped nest; 3 : Nesting material is completely shredded, nest walls have enough height to cover the entire animal; 4 : Nesting material is completely shredded, nest covers the entire animal including a complete roof. Nesting material was then removed from the cage and fresh nesting material ($\sim$7g = 3 Cotton nestlets) was added. The cage was then returned to the stabulation area and left untouched until the next day. Cage bedding was changed every week. For plugs, C57BL/6J female mice were housed either with a C57BL/6J male (regular mating) or with vasectomized Swiss male (for pseudopregnant females) overnight. A vaginal plug was accessed on the following morning. Positive females were returned to their home cage and nest quality was scored every 24 hours.

### Fos Mapping

At E14-E16 for plugged females, or 1 to 2 weeks following isolation and daily scoring of nests, mice were habituated to a novel home cage suited for video recording for 24h in a video-recording room with separate lighting control. The cages were filled with half of the bedding from the previous home cage. On the dark phase preceding the recording, the nesting material was removed. At the beginning of the following light phase, the live video recording system was turned on and fresh nesting material was added to the cage ($\sim$7g = 3 Cotton nestlets (Serlab, France "Nestlets")). 1 hour following the initiation of nest-building behavior, mice were euthanized with an intra-peritoneal (IP) injection of Pentobarbital 200 mg/kg IP (Euthasol), briefly perfused with PBS (1X) ($\sim$10mL) and fixed with intracardiac perfusion of 4% PFA in PBS (1X) ($\sim$50mL). The brains were dissected and post-fixed for 2 hours at 4°C in 4% PFA in PBS (1X).

### Automated nesting segmentation

To automatically segment interaction with nestlets in mice, we designed, developed, and built an open field system inspired by the Live Mouse Tracker (LMT)(Chaumont et al., 2019) . Briefly, using a structured light-based RGB-D camera (Kinect V2, Microsoft) placed at 45 cm from the cages bedding and the PyKinect2 Python library (https://github.com/Kinect/PyKinect2), we recorded both color (RGB) and registered (8bit) depth videos at $\sim$15 fps each. The videos were then processed offline using the OpenCV Python library (https://opencv.org) to segment nest-building behavior automatically. The code for behavioral segmentation is available here: https://github.com/Tom-top/TopMouseTracker.

To extract bouts of nest-building behavior, we first transformed the RGB image's color space to HSV (easing the segmentation). The image was then blurred using a Gaussian kernel (5x5) (to reduce high-frequency noise) and thresholded to generate a binary mask of the nesting material. The resulting binary mask was cleaned up from small artefactual objects and filled using morphological filtering (respectively, opening and closing with a (5x5) kernel, three iterations). We then detected the contours of the cleaned binary mask and excluded any object with an area smaller than 200px$^2$. Finally, we determined the height of the nesting material by computing the mean pixel value (MPV) within the binary mask applied to the corresponding registered depth frame. We labeled as nest-building behavior any change in the MPV greater than 9*s$^{-1}$. Finally, nest-building bouts separated by less than 2s were merged.

### Parental nesting

Primiparous Cart-Cre (n=5) and Cart-WT (n=5) female mice were isolated and moved to a new home cage 3 days prior exposure. In the day of exposure, females were transferred into the behavior room, the former nest was removed and new nesting material (3 cotton nestlets) was added to their cages. After 2 hours, the recording started and 5 minutes of pre-stimulus activity was recorded. One P1 to P3 C57BL/6 pup, obtained from a synchronized litter, was added to each cage for one hour.

### Elevated plus maze

For the elevated plus maze experiments, animals were first habituated to the behavioral room for at least 15 minutes. The mice were placed in the center of the plus maze of dimensions 76 cm x 76 cm, raised 60cm above the ground. Behavioral recordings were performed for 10 minutes and automatically analyzed using the CleverSys software (http://cleversysinc.com/CleverSysInc/). https://www.any-maze.com

### Chemogenetics

Mice were habituated to the open field video tracking system for 24h before the experiment. The dark phase preceding the recording, nestlets were removed from the cage. At the onset of the light phase, CART-Cre mice expressing hM4D(Gi) were injected intraperitoneally (i.p.) between E15-16 with either saline (0.9% NaCl) or CNO (1 mg/kg) (Enzo Life Sciences, Inc.) dissolved in saline. The injection of CNO or saline was randomized for each mouse. Each mouse was then tested the following day with the other compound, saline or CNO. Fifteen to twenty minutes after the injections, we added 3 cotton squares ($\sim$7g) (Serlab) and recorded the behavior of the animals for at least 5 hours.

### Optogenetics

Two to three weeks after stereotaxic viral injection and cannula implantation, Cart-Cre mice expressing either jGCaMP7s or jGCaMP7s with ChrimsonR were connected to the patch cord (Doric lenses) by a quick release interconnect (ADAL3; Thorlabs) and were habituated to the recording setup for at least 1 week. All optogenetic stimulations (10 ms pulses, at 20 Hz) were generated

# Neuron
## Article

**CellPress**
OPEN ACCESS

using Doric's system (Doric Lenses). The light was bandpass filtered at 593 nm (Doric lenses YBPF 593/040). We adjusted the light power exiting the tip of the patch cord to 5 mW. The protocol used for photostimulation consisted of 5 trains of 30s each with an inter-trial interval of 5 minutes for 1 hour. This protocol was then repeated 5 times between ZT20 and ZT2.

### Fiber photometry

Two to three weeks after viral injection and cannula implantation, Cart-Cre mice expressing jGCaMP7s were connected to the patch cord (Doric lenses) by a quick release interconnect (ADAL3; Thorlabs) and were habituated to the recording setup for at least 1 week. Over a period of 3 to 12 weeks after surgery, we recorded fluorescence signals from freely behaving mice in their home cages using Doric's fiber photometry system (Doric Lenses). Each recording session started at the beginning of the light phase (ZT-0). Excitation light (50μW at the tip) was supplied by a violet (405 nm) and a blue (490 nm) fiber-coupled light-emitting diodes, sinusoidally modulated at 531 and 211 Hz respectively. The light was passed down into a low-fluorescence patch cord (400 μm, 0.48 N.A; Doric Lenses) connected to the implanted optic cannula (400 μm, 0.48 N.A; Doric Lenses) by a quick release interconnect (ADAL3; Thorlabs). The fluorescence emission was then demodulated using lock-in amplifier detection. Signals were collected at 240 Hz using the Doric neuroscience studio software (Doric Lenses).

Analysis was performed using a custom Python script inspired by a previously published method (Vesuna et al., 2020). Briefly, both the 410 and 465 nm channels were first smoothed using a convolution of a scaled window with the signals (width ~400 ms). The smoothed 410 nm signal was regressed using non negative robust linear regression (least absolute shrinkage and selection operator (LASSO) algorithm) onto the 465 nm signal, and the regression coefficients were used to scale the 410 nm signal to the 465 nm one. The scaled 410 nm signal was then subtracted from the 465 nm signal. Finally, the z-score of the resulting signal was calculated.

### QUANTIFICATION AND STATISTICAL ANALYSIS

Significance levels indicated are as follows: * $P < 0.05$, ** $P < 0.01$, *** $P < 0.001$ and **** $P < 0.0001$. All data are presented as mean ± SEM. All statistical tests used were two-tailed. Investigators were blind to the experimental conditions. Multivariate data was analyzed by non-parametric one-way ANOVA (Kruskal-Wallis test) with Dunn's multiple comparisons test (Figures 1C and 4B) and two-way ANOVA with Tukey-Kramer's multiple comparisons test (Figure 3C(left and middle panel)). Comparisons between two conditions were mainly analyzed by unpaired Mann-Whitney ranked U test (Figures 1A, 1F, 1G, 4C, 5A, 5B (third and fourth panels), 5D-5F, 6G, 6I, 6J, 6L, 7B, 7C, S1C, S1F-G, S5A–S5E, S6C, S7B, S7D, S8A-B, and S8D), except the voxel-based statistics and region-based analysis performed with ClearMap, using Student's T-test (Figures 2D-E, , 8I-J and S2A). Paired analysis was done with Wilcoxon's signed rank test (Figures 1B, 7A (first and second panels), 6C, 6F, 6K, S6A-6B, S6E). In Figure 3C (right most panel), statistical analysis for the linear least-squares regression was performed using Wald's test with t-distribution of the test statistic. Statistical analysis was performed using R through Python 3.8 (rpy2, scipy) and GraphPad PRISM version 8.2.0. Python 3.8 (matplotlib) was used for the generation of graphs.